

Valley field mechanics: a local perspective beyond valley flavor

Feng-Wu Chen¹, Zheng-Han Huang¹, and Yu-Shu G. Wu^{1,2}

¹ Department of Electrical Engineering, National Tsing-Hua University, Hsin-Chu 30013, Taiwan

² Department of Physics, National Tsing-Hua University, Hsin-Chu 30013, Taiwan

ABSTRACT

Valleytronics in 2D materials is rooted in the existence of valley flavor but extends far out to the rich dimension of local physics, with abundant noteworthy twists with respect to valley flavor-based expectations, as demonstrated in this work. In order to explore the dimension, a Ginzburg-Landau order parameter type field – *valley field* is introduced. The field describes *local cell-orbital magnetic moment*, with the moment operationally defined irrespective of electron state energy in terms of local magnetic response and, thus, free from such ambiguity issue as encountered in defining the valley flavor of non-band-edge states. A theoretical framework – *valley field mechanics* which comprises valley fields and field equations of variant Schrodinger or Klein-Gordon forms is developed to analytically address the local physics and provides an intermediate-level quantum description interpolating between the valley flavor and primitive wave mechanics. Within the framework, the local linear response of a valley field to space-dependent magnetic and electric fields is discussed. It illustrates the existence of *local valley-Zeeman* and *local valley-orbit-interaction* effects and, thus, opens a path to *local valley control*. Numerical results of valley fields are presented, in bulks, quantum dots, quasi-1D structures, and structures with interfaces of gap inversion, of graphene and transition metal dichalcogenides. A variety of intriguing local phenomena are revealed with characteristics in apparent contradiction to valley flavor-based expectations and/or constraints, for example,

– broken “valley flavor \leftrightarrow magnetic moment orientation” correspondence,

– nonvanishing local magnetic moments in the presence of inversion symmetry,

– suppressed or even eliminated valley magnetic moments in the presence of broken inversion symmetry.

By revoking such expectations and/or constraints, the local physics enables a much more flexible valley control, and favorably relaxes both symmetry and material restrictions, with *gapless, single-layer graphene* – material with inversion symmetry, for example, added to the list for valley-based applications. Overall, the diverse local valley phenomena revealed suggest the exciting direction of *valley field engineering* - design and search for quantum structures to tailor local valley physics for applications.

I. Introduction

Following pioneering studies of quantum Hall effect in graphene layers [1–3], atomically thin 2D hexagonal crystals – gapped graphene [4–7] and transition metal dichalcogenides (TMDCs) [8,9] with broken inversion symmetry have soon been recognized to form an important class of topological materials [10,11], with a wide spectrum of novel phenomena present in association with the existence of two degenerate and inequivalent band structure valleys (K and K’). Studies have led to the exciting discovery of valley magnetic moments [10], valley Hall effect [10] with nonlocal resistance [12–15], robust valley topological currents [16–22], robust valley-polarized interface states [16], valley selection rule in optical pumping [9,23–26], spin-valley locking [11], valley-Zeeman [10] and valley-orbit interactions [27], and so on, and have fueled important device proposals for valleytronic applications – valley filters / valves [19,28,29], qubits [27,30–33], FETs [34] and etc. in versatile structures including graphene [35–42] and TMDC [13,43–48] quantum dots (QDs) / quasi-1D (Q1D) structures.

States of topological materials are generally characterized by nontrivial global quantities, for instance, Chern number, Z_2 invariant etc. – topological numbers of

ground state manifolds or energy bands in wave vector (\vec{k})-space, depending on the material. Topological protection in such materials can often lead to phenomenal effects such as extremely long state coherence vital for the applications of spintronics and topological quantum computing [49–52], as well as robust surface metallic states in 2D [53] and 3D [54,55] and end states in Q1D [56–59] in the presence of topological boundaries.

In the case of 2D hexagonal crystals, the topology is summarized by a ‘valley Chern number’ - essentially the integral of Berry curvature around a valley in the band structure. For crystals lacking inversion symmetry, valley Chern numbers are nonvanishing with opposite signs between K and K’ [16] alluding to the presence of some nontrivial topology. **Figure 1** illustrates the topology from a symmetry perspective and also inversion symmetry breaking in the crystal, in the case of gapped single-layer graphene (with gap = 2Δ).

Figure 1 shows the graphene crystal structure on the left hand side, where two types of atomic sites, A and B, are present and alternately occupy hexagonal vertices ($A = B = \text{carbon}$). Inversion symmetry breaking results from the two types of sites having distinct on-site atomic orbital energy (e.g., $\Delta \neq 0$). When $\Delta = 0$, the inversion symmetry is restored and the gap

vanishes as well. The crystal shown in the graph can describe TMDCs as well, with the assignment where A = metal atom, e.g., Mo, W and B = chalcogen atom pair, e.g., S₂, Se₂, for example.

Figure 1 shows the band structure on the right hand side, along with band edge state symmetry with respect to three-fold rotations and mirror reflection about the plane, which are elements of the crystal symmetry group (C_{3h}). [60] Depending on how band edge states transform under foregoing symmetry operations, they are classified into E'' or A'' states, and represented by (x+iy)z, (x-iy)z, or z to indicate corresponding state symmetry. As shown in the graph, the symmetry varies in the band structure, manifesting a twist between the valleys as well as across the gap. From the topological standpoint, the twist is similar to that in a Möbius strip, and signifies nontrivial topology in the fiber bundle formed of wave vector (\vec{k}) parametrized electron states in Hilbert space. Such twist reduces electron intervalley scattering, protecting valley flavor and enhancing valley lifetime for valley-based applications.

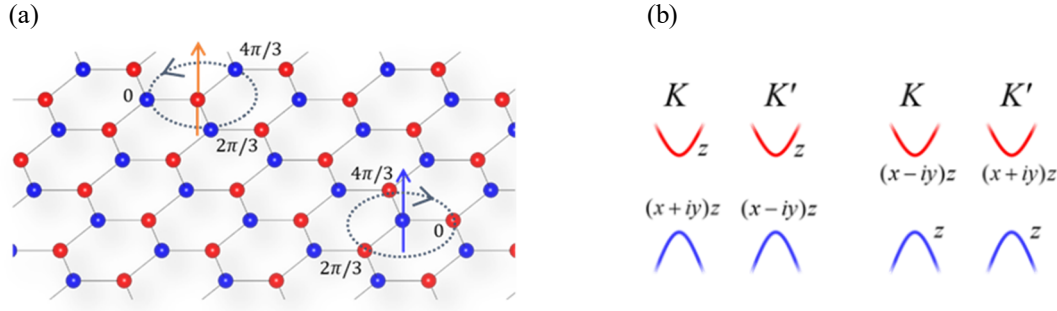


Figure 1. State symmetry twist and inversion symmetry breaking Gapped single-layer graphene is used for illustration. **(a)** With on-site 2p_z orbital energy $\varepsilon_A = \Delta$ for A site (red atom) and $\varepsilon_B = -\Delta$ for B site (blue atom), it breaks the inversion (A \leftrightarrow B) symmetry giving a gapped band structure (gap = 2 Δ) along with A (B) site orbital-dominated conduction (valence) band edge states [3], with phases of the states shown in the graph and explained in **(b)**. **(b)** Band structure is presented along with band edge state symmetry with respect to the crystal symmetry group C_{3h} symmetry operations consisting of three-fold rotations and mirror reflection about the plane, in the case where the center of rotation is an A site (left panel) and a B site (right panel). Under a rotation about A (B) site, valence (conduction) band edge states at K, for example, belong to the E'' irreducible group representation and transform with $\phi_{K(\text{valence})} \sim (x+iy)z$ ($\phi_{K(\text{conduction})} \sim (x-iy)z$) giving a phase increment $2\pi/3$ ($-2\pi/3$) around the red (blue) out-of-plane arrow as shown in **(a)**. Under a rotation about B (A) site, valence (conduction) band edge states at K belong to the A'' irreducible representation and transform with $\phi_{K(\text{valence})} \sim z$ ($\phi_{K(\text{conduction})} \sim z$). Altogether, the state symmetry is twisted across the gap and between the valleys.

by the existence of twist topology-induced property ‘COMM’. As a local magnetic moment, it can interact with external magnetic and electric fields, and manifest local field effects suited to the role of theoretically and experimentally guiding the exploration of local valley physics. Moreover, COMM is shown to give a measure of inversion symmetry breaking as well. In this work, a Ginzburg-Landau order parameter type field variable – *valley field* is thus defined in terms of the COMM distribution in \vec{r} -space, in order to provide a representation of local valley physics.

Analytically, a framework - ‘*valley field mechanics*’ centering on the valley field and corresponding field equation is developed. Both one and two energy band-based pictures are

Additional important implications follow from the twist topology. As unveiled in this work, it leads to a nontrivial property termed ‘cell-orbital magnetic moment (COMM)’, which is a *local magnetic moment* due to spin-like, local orbital rotation on the intra-cell scale. It generally varies in \vec{r} -space with cells. In the case of a homogeneous bulk, it reduces to a uniform distribution, with sum total being the corresponding bulk valley magnetic moment with opposite signs for K and K’.

COMM has important significance for local valley physics. Consider topological materials. While examples of local, \vec{r} -space fields such as the Ginzburg-Landau superconducting order parameter do exist [61,62], one that derives from a topological number should be highly valued and worth pursuit. Such a field can provide the topological description in \vec{r} -space and benefit important studies such as those of inhomogeneous systems. As exemplified in materials with topological boundaries, inhomogeneity profoundly alters the physics creating robust surface states. In our study of 2D hexagonal crystals, such a pursuit is motivated and facilitated

applied to the development yielding, respectively, valley field equations of variant Schrodinger form suitable for TMDCs and variant Klein-Gordon form suitable for graphene. In terms of such equations, the local aspect of valley physics is explored, including local field effects. A new path – local valley control via space-dependent electric and magnetic fields is opened up. The effect of structural inhomogeneity on valley physics is investigated, both analytically and numerically. A variety of intriguing findings are revealed, as sketched below, with a fraction of them showing characteristics in apparent contradiction to the “valley flavor-based expectations and/or constraints” well established in the study of homogeneous bulk case and having long constituted core beliefs in the field of valleytronics.

1) Breaking of “valley flavor \leftrightarrow magnetic moment orientation” correspondence

In a homogeneous bulk, there a correspondence between the valley flavor and the sign of valley magnetic moment [10,11]. In inhomogeneous structures, however, the study of valley fields sends an important signal - apart from a space-modulated magnitude, *the sign of local magnetic moment can flip in space*.

2) Disappearing valley magnetic moments

Valley magnetic moments exist in a homogeneous bulk lacking inversion symmetry, with important physical manifestations [10–22]. However, the study of valley fields reveals a surprise – suppression or even elimination of sum totals of the fields (i.e., valley magnetic moments) for states near the Dirac point, in zigzag graphene nanoribbons with gap parameter $\Delta \neq 0$. Such a finding apparently violates the valley flavor-based expectation.

3) Valleytronics in materials with inversion symmetry

By either symmetry or topological arguments, valley magnetic moments vanish in an homogeneous bulk with inversion symmetry such as gapless graphene ($\Delta = 0$) [10–22]. Previously, therefore, valley control through magnetic moment-external field interactions was regarded impossible in such a material. However, as shown in our work, antisymmetric but finite COMM distributions exist in zigzag nanoribbons of gapless graphene, which can interact locally with space-dependent external fields thus revoking the ‘inversion symmetry breaking’ condition and enabling *local valley control-based valleytronics in materials with inversion symmetry*. This adds *gapless, single-layer graphene*, for example, to the family of suitable valleytronic materials and relaxes both the material and symmetry constraints.

4) Contrasting material dependence

The existence (lack) of spin-valley locking in TMDCs (graphene) marks a well-known contrast between the two materials [10,11,23–26]. From the local perspective, valley physics is found to exhibit the following additional material dependence – in TMDCs the valley field always shows a uniform sign in space while in graphene it shows versatile behaviors, including a possible sign flip.

5) Direct-Indirect band gap control

The presence of a non-odd potential in Q1D structures is found to have profound effects on band structures. In zigzag graphene ones, such effects are shown to result in the induction of indirect gap near a Dirac point. It implies the feasibility of direct-indirect gap control via an electric potential.

6) Valley field engineering

Valley fields in confined structures vary with boundaries, quantization, and types of structures. Therefore, they can be engineered. Such engineering can be integrated with local

valley control for versatile applications.

The presentation is organized as follows. In **Sec. II**, we discuss the notion of valley fields, both generically and in the Dirac model of graphene. **Sec. III** presents numerical results of valley fields in various structures, of graphene and TMDCs, with a focus on physical behaviors of the fields. **Sec. IV** turns attention to the framework of valley field mechanics – valley field equations both in the absence and in the presence of external fields, including a description of local valley-Zeeman and local valley-orbit interactions useful for local valley control. **Sec. V** provides conclusion and outlook. The **Appendices** provide the theory infrequently used in the study (in **Appendix A**), supply mathematical details of derivations (in **Appendices B** and **C**), and discuss secondary effects (in **Appendix D**). Specifically, **Appendix A** presents the one-band picture-based Schrodinger theory of valley fields. **Appendix B** develops the two-band picture-based Klein-Gordon theory of valley fields, in structures confined by abrupt, asymmetric boundaries. **Appendix C** builds up the Klein-Gordon theory of valley fields in space-dependent magnetic and electric fields. **Appendix D** presents a perturbation-theoretical treatment of valley fields in the presence of valley mixing.

II. Valley field: a local concept

Locality and correlation constitute a pair of notions that have marked several decades long, milestone developments in physics. At times they are deemed mutually exclusive, as in the example of epic research in locality principle vs. quantum correlation / nonlocality in multipartite systems, with the EPR paradox [63] and Bell inequalities [64–67] in the early focus of exploration. In the broad interpretation of the notions, however, diverse examples exist where they go hand in hand and provide descriptions complementary to each other, in the condensed matter systems with traditional symmetry-breaking ordered phases [68].

Consider a general, inhomogeneous ferromagnetic state, for instance. At its base is the ensemble of electron angular momenta – spins or atomic orbital ones, of subatomic or atomic length scales. Such angular momenta can interact, align themselves macroscopically breaking the continuous rotational symmetry, and form a magnetic ordered state, where the corresponding order parameter – a local field ($\vec{\phi}(\vec{r})$) is able to describe a spatially varying ordered state featured by a fluctuation correlation with temperature (T)-dependent characteristic length, e.g., $\xi(T) \propto |T - T_c|^{-1/2}$ in the Ginzburg-Landau ϕ^4 phenomenology [68].

We define the COMM distribution in \vec{r} -space as the local “valley field” to address both local and correlation aspects of valley physics. **Sec. II-1** starts with a qualitative description of COMM and elucidates its physics by illustrating the connection between COMM and both state symmetry and inversion symmetry breaking, using graphene as an example. **Sec. II-2** moves to quantify the concept of valley field. In particular, it considers extended states in smoothly modulated

structures of graphene, in the Dirac model, and derive an expression of the field. **Sec. II-3** turns to a generic definition of the field independent of the material. **Sec. II-4** provides a discussion of gauge invariance for the definition.

In our discussion below and throughout the work, we follow two conventions when referring to the electron wave vector. In the analytical discussion, which is mostly carried out within the Dirac model, the wave vector is defined relative to the Dirac point (K or K') used in the model. In the discussion of numerical results, which are all obtained with the full-zone tight binding model, the wave vector is defined with respect to the Brillouin zone center (Γ).

II-1. The symmetry perspective

In the case of graphene, COMM derives from the simultaneous spin-like, local electron orbital rotation while an electron performs global translation, as shown in **Figure 2**. Consider a near-K state, for example. Generally, it superposes the two components, namely, A site-dominant $\phi_{K(\text{conduction})}$ and B site-dominant $\phi_{K(\text{valence})}$ shown in **Figure 1**. As depicted in **Figure 2**, because the two have distinct E'' and A'' symmetry, they exhibit loop currents of opposite senses and compete. With each current carrying the weight of corresponding local probability, the competition yields $\text{COMM} \propto \rho_A - \rho_B$ ($\rho_{A(B)}$ = probability on A(B) site) as the result of a net, spin-like local rotation or 'local pseudospin'.

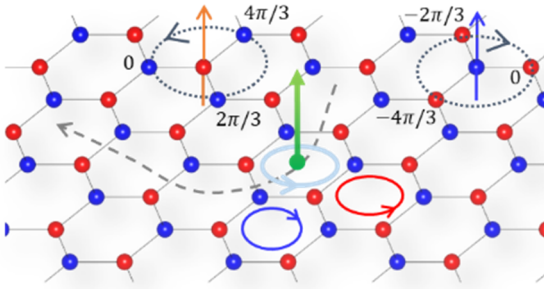


Figure 2. Cell-orbital magnetic moment Gapped single-layer graphene is used for illustration, with on-site energy $\varepsilon_A = \Delta$ for A site (red atom) and $\varepsilon_B = -\Delta$ for B site (blue atom). COMM describes the spin-like, local orbital rotation (light green circle) or 'local pseudospin' emergent from the competition between E'' and A'' symmetry while an electron simultaneously executes a global translation (grey dashed line). Consider a near-K state, for example. Generally, it superposes the two components – A site-dominant $\phi_{K(\text{conduction})}$ and B site-dominant $\phi_{K(\text{valence})}$, with E'' and A'' symmetry, respectively, as well as corresponding loop currents of opposite senses (orange and blue circles), resulting in the net current $\propto \rho_A - \rho_B$ (light green circle) and corresponding COMM (green, out-of-plane arrow). COMM thus describes i) the local dominant state symmetry (E'' or A'') and ii) probability-based inversion symmetry breaking.

Two important pieces of symmetry information are carried in COMM about the competition, as summarized below.

1) Local dominant state symmetry – E'' or A''

The sign of COMM indicates the local dominant state symmetry. Specifically, when ' $\rho_A - \rho_B$ ' changes sign between two regions, it signifies the occurrence in \vec{r} -space of a twist in the dominant symmetry.

2) Probability-based inversion symmetry breaking

In analogy to the Ginzburg-Landau symmetry-breaking order parameter ϕ , being proportional to ' $\rho_A - \rho_B$ ', COMM serves as the continuous parameter measuring 'probability-based inversion symmetry breaking', with $\text{COMM} = 0$ being the symmetry reference.

In summary, on the intra-unit cell scale, a finite COMM signals the existence of a net cell-orbital angular momentum or short-ranged phase correlation among intra-hexagon sites. On the inter-unit cell scale, the COMM distribution is a local field similar to the Ginzburg-Landau order parameter ϕ and can describe spatially varying, *probability-based* inversion symmetry breaking. These foregoing features thus inspire us to introduce the COMM distribution as the "valley field" to describe both local and correlation aspects of valley physics, with an aim at covering the physics in inhomogeneous systems.

Next, we turn to the Dirac model, quantify, and further discuss the concept of the field.

II-2. Valley field in the Dirac model

A gapped monolayer graphene structure is considered, in the linearized, two-band tight-binding model, also known as Dirac model, where the atomic $2p_z$ orbital per carbon atom is included in the basis set. [3] Generally, the structure is taken to be subject to the modulation of $V(x,y)$, $\Delta(x,y)$ and $B_z(x,y)$ ($V(x,y)$ = electrical potential energy; $2\Delta(x,y)$ = local bulk gap, with $\Delta = \Delta_0$ (constant) + $\delta\Delta$ (modulation); $B_z(x,y)$ = out-of-plane magnetic field with $(A_x(x,y), A_y(x,y), 0)$ the corresponding vector potential, (x, y) = cell position).

Let $F^t = (F_A, F_B)$ = transposed Dirac two-component wave amplitude on carbon A and B sites, valley index $\tau = 1$ (-1) for valley K (K'), and E = electron energy. In the Dirac model, F in external fields satisfies the following equation ($\hbar = 1$, $-e = 1$, and $v_F = 1$ (Fermi velocity) throughout the work) [3,27]:

$$H_{\text{Dirac}} F = EF, \quad (1)$$

$$H_{\text{Dirac}} = \begin{pmatrix} \Delta + V & -i\partial_x - A_x - \tau(\partial_y - iA_y) \\ -i\partial_x - A_x + \tau(\partial_y + iA_y) & -\Delta + V \end{pmatrix}.$$

Consider the relatively simple case of a weakly and smoothly modulated structure in the absence of external fields, where $V = 0$, $B_z = 0$, $|\delta\Delta| \ll \Delta_0$, and $|\nabla\Delta \cdot (\lambda_x, \lambda_y)| \ll \Delta_0$ ($\lambda_{x(y)}$ = electron characteristic wavelength in the x (y) direction). The above equation can be used to show that the

current distribution (\vec{j}) takes the following form conforming with that given in magnetostatics [69]:

$$\begin{aligned}\vec{j} &= \vec{j}_f + \vec{j}_m \\ \vec{j}_m &= \nabla \times \vec{m},\end{aligned}\quad (2)$$

where \vec{j}_f = free current distribution, \vec{j}_m = magnetization current distribution, and \vec{m} = magnetization distribution, with

$$\begin{aligned}\vec{j}_f &= \frac{-iF^\dagger \nabla F + i(\nabla F^\dagger)F}{2E}, \\ \vec{j}_m &= \tau \left(\frac{\partial_y \rho_{diff}}{2E}, -\frac{\partial_x \rho_{diff}}{2E} \right), \\ \vec{m} &= -\frac{\tau \rho_{diff}}{2E} \hat{z}\end{aligned}\quad (3)$$

($\rho_{diff}(x, y) \equiv \rho_A(x, y) - \rho_B(x, y)$, $\rho_{A(B)}(x, y) \equiv |F_{A(B)}(x, y)|^2$).

Extension of Eqn. (3) to the case where the modulation is sizable and/or external fields V and B_z are present will be given in **Sec. II-3**. Several important observations based on Eqn. (3) are made below:

- i) As $\vec{m} \propto \rho_{diff}$, we identify \vec{m} as the magnetic moment COMM due to local intra-cell orbital rotation described in **Figure 2**, and define m ($m \equiv \vec{m} \cdot \hat{z}$) as the valley field, with the sign of m indicating the local, dominant site orbital as well as state symmetry.
- ii) \vec{j}_f can be written in the form $\vec{j}_f(F_A) + \vec{j}_f(F_B)$, a site-decoupled sum where $\vec{j}_f(F_{A(B)})$ is the current distribution $\frac{-iF_{A(B)}^* \nabla F_{A(B)} + i(\nabla F_{A(B)}^*)F_{A(B)}}{2E}$ for one-component wave function $F_{A(B)}$. Since $\vec{j}_f(F_{A(B)})$ is determined by the inter-cell gradient $\nabla F_{A(B)}$, we identify \vec{j}_f as the *inter-cell translation current* due to the global translation described in **Figure 2**.

- iii) For a homogeneous bulk state ($\Delta = \Delta_0$), the Dirac model gives

$$\begin{aligned}\vec{j}_f &= \frac{\vec{k}}{E} \rho, \\ \vec{j}_m &= 0, \\ m &= \rho \mu_{bulk}(E, \Delta_0; \tau),\end{aligned}\quad (4)$$

$$\mu_{bulk}(E, \Delta_0; \tau) \equiv -\frac{\tau \Delta_0}{2E^2}$$

(\vec{k} = wave vector relative to the Dirac point, $\rho(x, y) \equiv \rho_A(x, y) + \rho_B(x, y)$, $\mu_{bulk}(E, \Delta_0; \tau)$ = valley magnetic moment of the bulk state). m in this case is simply the ρ -weighted distribution of μ_{bulk} in (x, y) space. Eqn. (4) can be alternatively obtained with

a topological, valley Berry curvature-based approach [10]. Importantly, it shows the two notable features of μ_{bulk} established in the field of valleytronics, namely, the correspondence between τ and the sign of μ_{bulk} , and vanishing μ_{bulk} in the presence of inversion symmetry ($\Delta_0 = 0$) [10]. Such features constitute what we call “valley-flavor based expectations or constraints” that have long guided the field when selecting materials or structures for exploration.

- iv) For fixed τ and E , gap inversion ($\Delta_0 \rightarrow -\Delta_0$) results in $\rho_{diff} \rightarrow -\rho_{diff}$ and, hence, valley field sign reversal ($m \rightarrow -m$). This fact will be useful when reading valley fields in the case of structures with gap inversion ($\Delta / -\Delta$) interfaces in **Sec. III**.

In numerical studies of this work, magnetic moments in confined structures are expressed in units of “ μ_B^* ”, the magnitude of bulk band edge valley magnetic moment in the well or channel of the structure. In graphene, for example,

$$\mu_B^* \equiv |\mu_{bulk}(E = \pm \Delta_{channel}, \Delta_{channel}; \tau)| = \frac{1}{2|\Delta_{channel}|} \quad (\Delta_{channel} =$$

bulk gap parameter in the channel). When $\Delta_{channel} = 0$, we use the Bohr magneton μ_B (5.79×10^{-5} eV/Tesla) in place of μ_B^* .

II-3. Generic definition

A model-independent, functional derivative expression of valley field is given in terms of the local response to a weak probing magnetic field as follows:

$$m(\vec{r}) = - \left. \frac{\delta E_{Zeeman_valley}[B_z^{(probe)}(\vec{r})]}{\delta B_z^{(probe)}(\vec{r})} \right|_{B_z^{(probe)}(\vec{r})=0}, \quad (5)$$

$$E_{Zeeman_valley}[B_z^{(probe)}(\vec{r})] = - \int m(\vec{r}) B_z^{(probe)}(\vec{r}) d^2 r$$

(E_{Zeeman_valley} = valley-Zeeman energy, $B_z^{(probe)}$ = probing magnetic field). Above two expressions are equivalent and exploit the physics of local Zeeman interaction to define $m(\vec{r})$.

The probing field is taken to be a hexagonal (strip) flux in the QD (Q1D) structure as shown in **Figure 3**. In the case of Q1D structure, usage of the strip flux results in $m(y)$ with translational symmetry in the x-direction, consistent with the existence of the same symmetry in the structure.

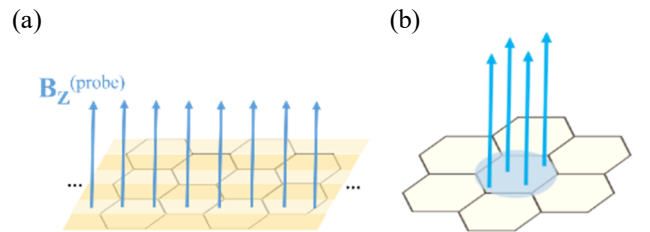


Figure 3. $B_z^{(probe)}$ (a) A strip of local, vertical magnetic field in the case of a Q1D structure. (b) A hexagonal magnetic flux in the case of a quantum dot.

While the valley-Zeeman energy E_{Zeeman_valley} in Eqn. (5) sums all the local valley-Zeeman energy ‘ $-m(\vec{r})B_z^{(probe)}(\vec{r})$ ’, it constitutes only a part of the total electron-magnetic field interaction energy, as expressed below:

$$E_{Zeeman_valley} = \begin{cases} E_{total} - E_{Zeeman_other} & \text{(QD)} \\ E_{total} - E_{Zeeman_other} - E_{Landau} & \text{(Q1D)} \end{cases}. \quad (6)$$

Above, E_{total} = total electron-magnetic field interaction energy, E_{Zeeman_other} = non-valley, e.g., spin Zeeman energy, and $E_{Landau} = -\langle A_x^{(probe)} \rangle \int \langle j_x \rangle dy$ (Landau orbital-magnetic field interaction energy). $A_x^{(probe)}(y)\hat{x}$ = probing vector potential in the asymmetric gauge, and $\langle \dots \rangle$ denotes the spatial average of expression inside the bracket. Eqn. (6) defines E_{Zeeman_valley} through a breakdown of E_{total} .

We note a few points below:

- i) $m(\vec{r})$ in the 2D bulk is covered by the Q1D expression above in the wide structure limit.
- ii) When applied to graphene of the Dirac model, the generic definition can be shown to recover the valley field expression given in Eqn. (3).
- iii) For Q1D structures, Eqn. (5) leads to the following magnetization current in the x-direction:

$$\partial_y m(y) = j_x(y) - \left[\int \langle j_x \rangle dy \right] \rho(y). \quad (7)$$

This generalizes Eqn. (3) to the case where external fields are present, and so is valuable to the analytic treatment of field effects on m , such as those presented in **Sec. IV** and **Appendix C**. For example, in the case of graphene structures, in the presence of potential energy $V^{(v)}(y)$ and vector potential $A_x(y)$, the current distribution $j_x(y)$ is given by ($\hbar=1$, $-e=1$, $v_F=1$):

$$j_x(y) = \left(\frac{k_x - A_x(y)}{E - V^{(v)}(y)} \right) \rho(y) + \left(\frac{\tau}{2[E - V^{(v)}(y)]} \right) \partial_y \rho_{diff}(y), \quad (8)$$

as can be verified with the Dirac wave equation (1). With Eqn. (8), Eqn. (7) gives an equation of $m(y)$ in the presence of external fields, allowing for the study of field effects.

- iv) Eqns. (5) and (6) are also useful to numerical studies of m . In our numerical work, for example, the various

energy terms involved in the equations are obtained via a tight-binding model-based band structure calculation where the magnetic field $B_z^{(probe)}(y)$ is included by Peierls substitution in the model [70].

$m(\vec{r})$ defined above is gauge invariant, as development of the foregoing expression for $m(\vec{r})$ has been guided by applying the principle of *gauge invariance*. This is explained next.

II-4. Gauge invariance

We discuss Q1D structures first, and QDs next. For simplicity, we exclude *non-valley magnetic moments* such as spin ones from the discussion.

Q1D structures

With non-valley magnetic moments excluded, we write $E_{Zeeman_valley} = E_{total} - E_{Landau}$. In principle, E_{total} can be obtained from the following electron-magnetic field interaction energy integral

$$E_{total} [B_z^{(probe)}(y)] \equiv - \int j_x(y) A_x^{(probe)}(y) dy. \quad (9)$$

However, it is obvious that such an integral is generally gauge dependent, which may thus require suitable discretion to avoid causing gauge dependence in E_{Zeeman_valley} and, consequently, in m . On the other hand, the gauge dependence in Eqn. (9) is useful as it can guide the search for a suitable expression of E_{Landau} that offsets the gauge dependence in E_{total} to achieve gauge independence in $E_{total} - E_{Landau}$, i.e., E_{Zeeman_valley} .

In both analytical and numerical studies, we use the asymmetric Landau gauge that preserves the lattice translation symmetry in the x-direction. So, the only allowed gauge transformation is the uniform shift: $A_x^{(probe)}(y) \rightarrow A_x^{(probe)}(y) + A_0$ (A_0 = arbitrary constant). With the following expression

$$E_{Landau} [B_z^{(probe)}(y)] \equiv - \langle A_x^{(probe)} \rangle \int \langle j_x \rangle dy, \quad (10)$$

it yields an A_0 -independent expression of E_{Zeeman_valley} , as can be verified easily.

Quantum dots

In quantum dots,

$$\begin{aligned} \vec{j}_f \text{ (free current)} &= 0, \\ \vec{j} &= \vec{j}_m \text{ (magnetization current)} = \nabla \times \vec{m}. \end{aligned} \quad (11)$$

With Eqn. (11), Eqn. (9) becomes

$$E_{total} [B_z^{(probe)}(x, y)] = - \int m(\vec{r}) B_z^{(probe)}(\vec{r}) d^2 r \quad (12)$$

Since the above right hand side is explicitly a functional of $B_z^{(probe)}(x, y)$, gauge independence of $E_{total} [B_z^{(probe)}(x, y)]$ is ensured. Moreover, it shows $E_{Zeeman-valley} [B_z^{(probe)}(y)] = E_{total} [B_z^{(probe)}(y)]$ in this case, reproducing Eqn. (6) in the case of QDs when non-valley magnetic moments are excluded.

III. Valley field: physical behaviors

Due to the topological distinction between open and compact spaces, a new realm of valley phenomena beyond the single valley Chern number description or valley flavor-based expectations may arise in QD / Q1D structures.

In this section, physical behaviors of valley fields are discussed in confined structures of the following classes, respectively:

- i) barrier-confined graphene structures,
- ii) confined TMDC structures,
- iii) graphene structures with gap inversion ($\Delta / -\Delta$) interfaces,
- iv) graphene structures confined with abrupt, asymmetric boundaries,
- v) structures with valley mixing.

These structures are selected to show 1) unique local phenomena contradicting “valley-flavor based expectations”, in the case of Classes **i**) and **iv**); or 2) contrast between TMDCs and graphene in local valley physics, in the case of Class **ii**); or 3) local valley physics in structures of current research interest, in the case of Class **iii**), where topological boundaries are present; or 4) the effect of valley mixing on local valley physics, in the case of Class **v**).

For insights into the physics, materials and structures considered are relatively ideal and simple. For example, graphene is taken to be monolayered and Δ -modulable [4]. QDs are taken to be square ones, with the armchair (zigzag) axis running in the x (y) direction. Q1D structures are oriented in the x-direction in our convention.

In the structures considered, while edge states are known to exist in those with abrupt boundaries [3], they are surface properties generally sensitive to chemical treatment and passivation. As such, the discussion of valley fields is focused on “non-edge states” throughout the work.

Sec. III-1 describes a reference, one-band-based physical picture. **Sec. III-2** presents numerical results.

III-1. Reference picture

One-band picture

As a reference, we introduce the zeroth-order picture based on one-band effective mass approximation for smoothly modulated structures [27]. It writes a near-band-edge state ψ of conduction or valence bands in the form

$$\psi(x, y) \approx f(x, y) \phi_\tau(x, y) \quad (13)$$

($f(x, y)$ = slowly varying envelop function, $\phi_\tau(x, y)$ = band-edge Bloch state of valley τ). Eqn. (13) describes the state as being locally given by $\phi_\tau(x, y)$, with an overall amplitude subject to the global modulation of $f(x, y)$. It suggests for the valley field the following corresponding expression:

$$m(x, y) \sim \rho(x, y) \mu_\tau, \quad (14)$$

where μ_τ is the valley magnetic moment of band edge state $\phi_\tau(x, y)$ (e.g., $\mu_\tau = \mu_{bulk}(\Delta_0, \Delta_0; \tau)$ in graphene), with an overall magnitude subject to the modulation of probability distribution $\rho(x, y)$ ($\rho(x, y) = |f(x, y)|^2$).

Eqn. (14) describes the one-band picture of $m(x, y)$, which is virtually a local generalization of the homogeneous bulk expression stated in Eqn. (4). It implies relatively simple, monotonous valley fields, with a uniform sign in space, a strong correlation between m and ρ , a “ $\tau \leftrightarrow$ sign of m ” correspondence etc., which are well within “valley-flavor based expectations” described in Eqn. (4).

Generally, the one-band description works reasonably well when electron states involved are, on the band gap energy scale, sufficiently near the band edge. From such a perspective, the description is generally suitable for TMDCs. Given their relatively wide band gaps (O(eV)) and heavy effective masses [8,9], typical electron states of interest in this case, including those in confined structures, are sufficiently close to the band edge. As can be verified later in **Sec. III-2**, the description along with valley flavor-based expectations generally holds for TMDCs.

Beyond the picture

Graphene typically has a relatively narrow gap (O(10-100 meV)) [4-7] and light effective mass. Therefore, with respect to the band gap scale, electron states involved may be relatively away from both conduction and valence band edges. In a weakly and smoothly modulated structure, including the homogeneous bulk, as discussed in the Dirac two-band model in **Sec. II-2**, the corresponding $m(x, y)$ is determined by both ‘ ρ_A ’ and ‘ ρ_B ’, with $m \propto \rho_A - \rho_B$.

In the case of confined states, however, standing waves on A sites and on B sites may oscillate with distinct phases and wavelengths, leading to separate fluctuations in ‘ ρ_A ’ and ‘ ρ_B ’. Breakdown of the one-band picture may thus happen, with the degree of breakdown depending on the state energy and structure involved. The breakdown can sometimes become dramatic: when the crossover “ $\rho_A / \rho_B > 1 \leftrightarrow \rho_A / \rho_B < 1$ ” occurs in space, it even leads to the manifestation of a sign flip in m .

Two mechanisms listed below strongly differentiate sites A and B and, hence, contribute to the above oscillation contrast:

- i) asymmetric boundaries – in the case of a zigzag nanoribbon, the two boundaries terminate at A and B

- ii) sites, respectively;
 on-site atomic orbital energy difference between A and B sites.

Overall, the one-band picture will serve as a guide in **Sec. III-2** to identify bulk-like or valley flavor-based behaviors. More importantly, breakdown of the picture will be used to pinpoint the modulated structure-specific behaviors that are beyond the reach of single valley Chern number description. Where the breakdown occurs, a relatively sophisticated two-band approach is required in place of the one-band picture to provide a suitable description, which can be the Dirac model used in **Sec. II-2** or the two-band-based Klein-Gordon theory introduced later in **Sec. IV**.

III-2. Numerical results

For the numerical work, we apply the tight-binding model of graphene with $2p_z$ orbital per carbon in the atomic orbital basis set [71] and that of TMDCs with $3d\uparrow/\downarrow$ orbitals per metal atom in the set [72,73]. In both models, only nearest neighbor hopping between the orbitals are included.

i) Barrier-confined graphene structures

Figure 4 illustrates general features of quantum confined valley fields. A zigzag graphene Q1D structure confined with barriers is considered, with dimensions given by $W_{\text{barrier}} = 65.2 a$ (barrier width) and $W_{\text{channel}} = 65.8 a$ (channel width), and bulk

gap parameters $\Delta_{\text{barrier}} = 0.3 \text{ eV}$ and $\Delta_{\text{channel}} = 0.1 \text{ eV}$ ($a =$ bulk lattice constant). The graph presents the result of valley fields in the case of top and second valence subbands. **(a)** and **(b)** show corresponding sum totals of the valley fields (termed valley magnetic moment here and throughout the work, by analogy with the homogeneous bulk case) vs. k_x and varying W_{channel} , respectively. **(c)** shows the valley field and probability distribution ($\rho(y)$) of the top valence subband state at Dirac point. **(d)** shows $\rho_A(y)$ and $\rho_B(y)$ of the foregoing state. **(e)** shows the valley field and $\rho(y)$ of the second valence subband state at Dirac point. **(f)** shows $\rho_A(y)$ and $\rho_B(y)$ of the foregoing state.

Overall, the figure demonstrates a strong correlation between valley field and $\rho(y)$, in the case of the top subband state, as well as breakdown of the correlation when going to deeper valence subbands. In particular, it shows why the sign variation is absent (present) in the case of top (second) subband state: $\rho_A(y)$ and $\rho_B(y)$ oscillate with different phases and wavelengths, ending up with a uniform (varying) sign in $\rho_A(y) - \rho_B(y)$ and, hence, valley field, too, in the case of top (second) subband state.

Structures with armchair edges – QDs and armchair Q1D structures involve intervalley coupling and will be discussed later in the category of ‘structures with valley mixing’.

Zigzag graphene Q1D structure

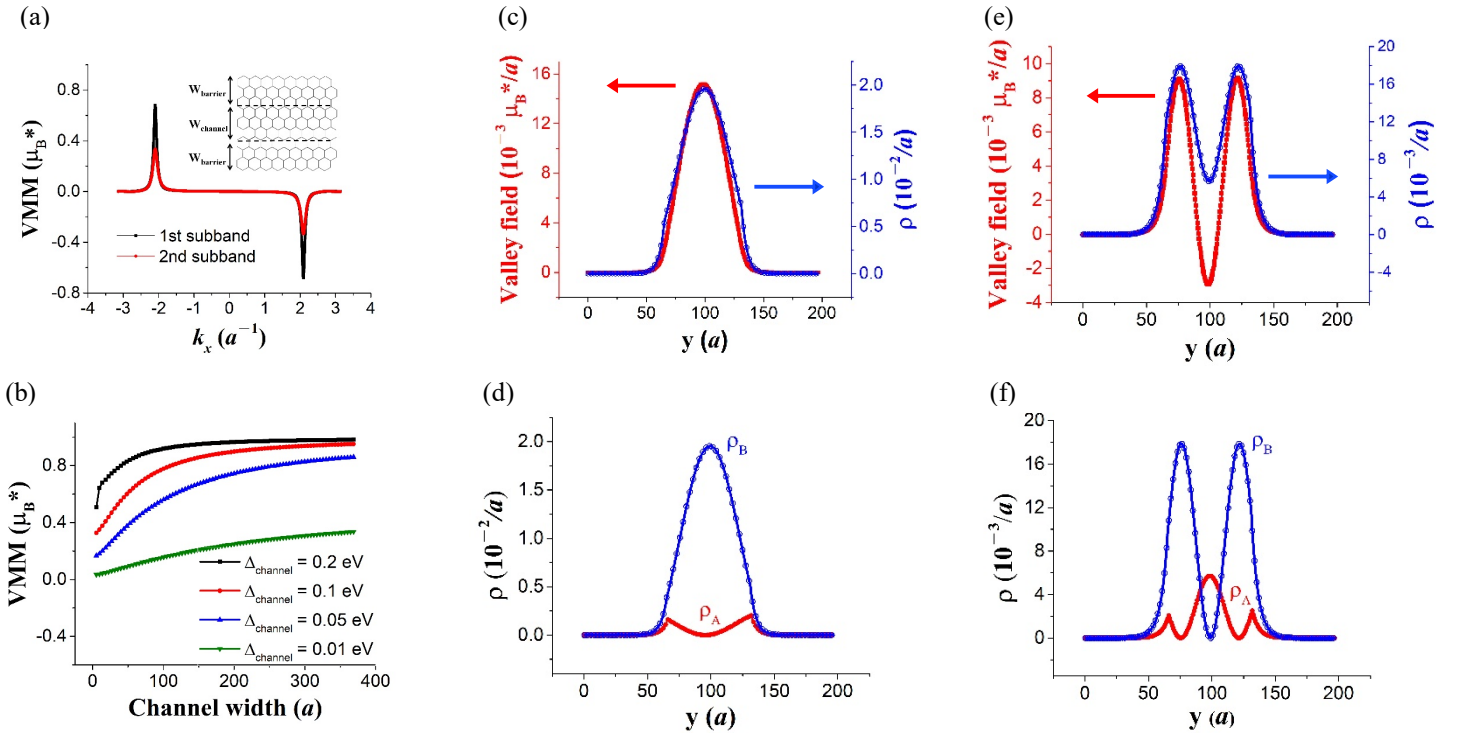


Figure 4. Valley fields in Zigzag graphene Q1D structure **(a)** Valley magnetic moment (VMM) vs. k_x , of the first and second valence subbands. **(b)** VMM of the first valence subband state at Dirac point ($k_x \sim -2.10 a^{-1}$) vs. channel width (W_{channel}) as well as gap (Δ_{channel}). It approaches the bulk limit μ_B^* when either W_{channel} or Δ_{channel} increase. **(c)** Valley field and probability distribution ($\rho(y)$) of the top valence subband state at Dirac

point. **(d)** $\rho_A(y)$ and $\rho_B(y)$ of the state in **(c)**. **(e)** Valley field and $\rho(y)$ of the second valence subband state at Dirac point. **(f)** $\rho_A(y)$ and $\rho_B(y)$ of the state in **(e)**. **(c-f)** shows a strong correlation between the sign and magnitude of valley field and those of $\rho_A(y) - \rho_B(y)$. **(c)** and **(d)** are well described by the one-band picture. While in **(e)** and **(f)**, with standing waves of A and B sites oscillating in separate phases and wavelengths, the crossover “ $\rho_A / \rho_B > 1 \leftrightarrow \rho_A / \rho_B < 1$ ” occurs in y along with the manifestation of a sign flip in valley field. A coarse grain averaging is performed in both the valley field and $\rho(y)$ here as well as throughout the work, in the case of Q1D structures, unless noted otherwise.

ii) TMDC structures

For TMDCs, we focus on valence band states, as they carry an important potential for valley-based applications due to the presence of strong spin-valley-orbital locking and correspondingly induced valley protection [11,74]. For a similar reason, we pick WSe₂ as the material. It has, for example, a larger spin-orbit coupling than MoSe₂ and a wider K- Γ energy separation than WS₂ [75], both of which result in a better protection for the valley flavor in the material.

Figure 5 shows valley fields and probability distributions of the top valence non-edge QD-confined state in two rectangular QDs with different aspect ratios. In **(a)**, $W_x = 9.53 a$ and $W_y = 13 a$. The energy of the state is 0.126 eV, with valley magnetic moment (VMM) = $0.76 \mu_B^*$. In **(b)**, $W_x = 19.9 a$ and $W_y = 6 a$. The energy of the state is 0.037 eV, with VMM = $0.62 \mu_B^*$. μ_B^* here is the VMM of valence band edge state at Dirac point in bulk WSe₂, which is about $4.1 \mu_B$ [74]. Note that, because of spin-valley-orbital locking, the Kramers two-fold

valley degeneracy is protected from the armchair edge induced inter-valley scattering. For demonstration, we choose the valley state with positive VMM to present in the figure.

Figure 6 shows the valley field in a zigzag WSe₂ Q1D structure confined with barriers, with $W_{\text{channel}} = 21.7 a$ and $W_{\text{barrier}} = 30.3 a$. **(a)** shows the subband structure. **(b)** shows VMM vs k_x for each subband. **(c)** shows the valley field and $\rho(y)$ of the top valence subband state at Dirac point. Note that, because of valley degeneracy, we again choose the valley state with positive VMM for demonstration.

Overall, in both **Figures 5** and **6**, a strong correlation is illustrated between the valley field and probability distribution. Because of the spin-valley-orbital locking protection, the correlation illustrated is expected to be present independent of confining boundary types – abrupt edges or finite barriers, as well as edge orientations - zigzag or armchair ones, as is indeed confirmed in our study (not shown here).

WSe₂ quantum dots

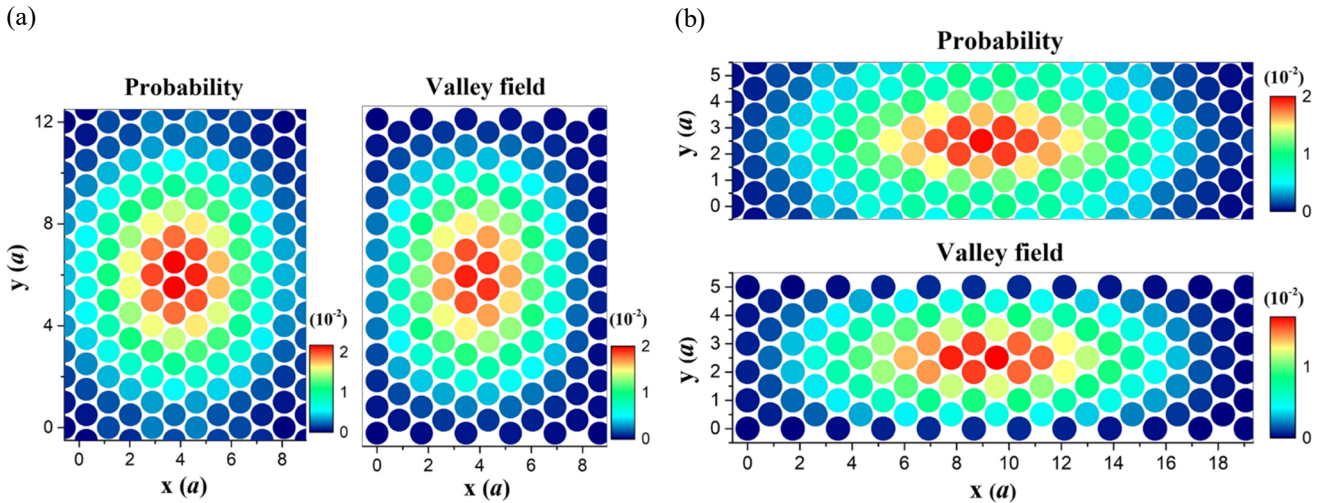


Figure 5. Valley fields in TMDC quantum dots Valley fields (in units of $\mu_B^*/(\text{hexagon area})$) and probability distributions ($\rho(x, y)$) of the top valence non-edge QD-confined state in rectangular WSe₂ QDs confined with abrupt boundaries, for two different aspect ratios. In **(a)**, $W_x = 9.53 a$ and $W_y = 13 a$. The energy of the state is 0.126 eV, with valley magnetic moment (VMM) = $0.76 \mu_B^*$. In **(b)**, $W_x = 19.9 a$ and $W_y = 6 a$. The energy of the state is 0.037 eV, with VMM = $0.62 \mu_B^*$. μ_B^* is the VMM of valence band edge state at Dirac point in bulk WSe₂, which is about $4.1 \mu_B$ [74]. Due to the lack of reflection symmetry about the QD vertical center line, probability distributions and valley fields are slightly asymmetric in both **(a)** and **(b)**. Overall, the correlation is observed to be present independent of confining boundary types – abrupt edges or finite barriers (not shown).

Zigzag WSe₂ Q1D structure

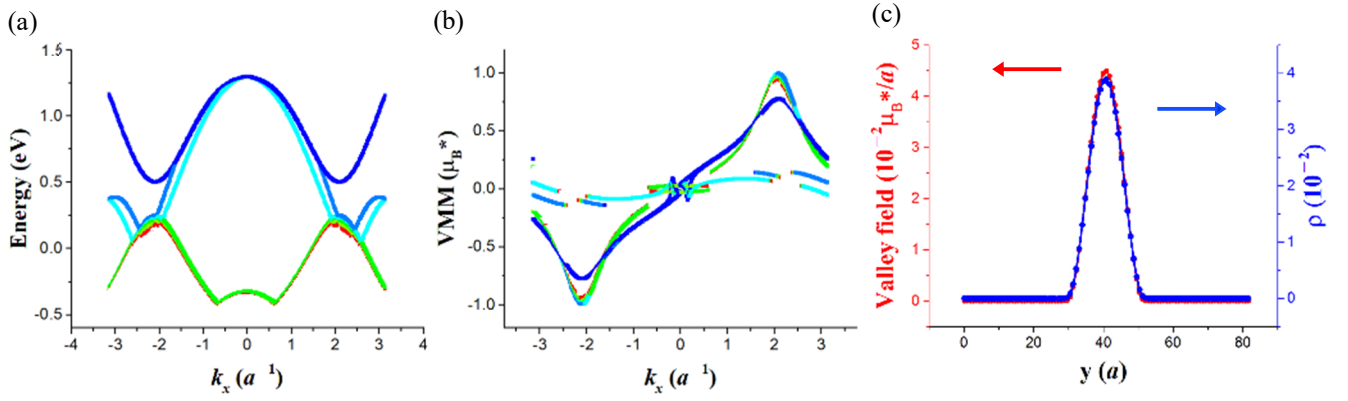


Figure 6. Valley fields in Zigzag WSe₂ Q1D structure A zigzag WSe₂ Q1D structure confined with barriers is considered, with width parameters $W_{\text{channel}} = 21.7 a$ and $W_{\text{barrier}} = 30.3 a$. In order to confine holes to the channel, a negative on-site potential energy (-1 eV) is introduced to form barriers on both sides of the channel. **(a)** Subband structure. **(b)** Valley magnetic moment (VMM) vs k_x for each subband. **(c)** Valley field and $\rho(y)$ of the top valence subband state at Dirac point. The color in **(a)** and **(b)** is used as band index. The barrier potential lowers surface bands into the range of valence subbands and produces band crossings. Due to such crossings, **(b)** shows discontinuity in several colored curves. Overall, the correlation is observed to be present independent of confining boundary types – abrupt edges (not shown) or finite barriers, as well as orientations - zigzag or armchair (not shown) ones.

iii) Graphene structures confined with abrupt asymmetric boundaries

Zigzag nanoribbon cases are presented to illustrate the profound effect of asymmetric boundaries on topology, in **Figures 7 and 8**. The two figures feature electron states in gapless and gapped zigzag ribbons with gap parameters $\Delta = 0$ eV and $\Delta = 0.1$ eV, respectively, and the same width $W = 65.8 a$.

In **Figure 7**, **(a)** shows the subband structure. **(b)** shows the valley field accumulated over half width of the ribbon ($\text{VMM}_{1/2}$) vs. k_x for each subband. **(c)** depicts valley fields of a few second subband states ($k_x = -1.88 a^{-1}$, $-2.10 a^{-1}$, $-2.31 a^{-1}$) in the neighborhood of Dirac point. **(d)** shows $\rho_A(y)$ and $\rho_B(y)$ of the state at Dirac point ($k_x = -2.10 a^{-1}$), implying a sign oscillation in $\rho_{\text{diff}}(y) = \rho_A(y) - \rho_B(y)$ and, hence, in corresponding valley field, too, which is consistent with what is shown in **(c)**.

Overall, in the gapless case presented in **Figure 7**, valley fields are shown to be always antisymmetric in y , thus resulting in vanishing valley magnetic moments independent of k_x . However, the field accumulated over half width of the ribbon ($\text{VMM}_{1/2}$) is significant and can sometimes exceed $10 \mu_B$ to provide an access to local valley control, as discussed later in **Sec. IV-2**.

In **Figure 8** of the gapped case, **(a)** shows the top two valence subbands. **(b)** shows valley magnetic moment (VMM)

vs. k_x for the two subbands, which reveals vanishing VMMs for edge states (flat part of blue curve in **(a)**), and an overall suppression of VMM near each Dirac point, in the case of second valence subband. **(c)** presents the valley field and $\rho(y)$ of the second subband state at Dirac point. The corresponding $\rho_A(y)$ and $\rho_B(y)$ of the state are shown in **(d)**, which imply a sign oscillation in $\rho_{\text{diff}}(y) = \rho_A(y) - \rho_B(y)$ and, hence, in corresponding valley field, too, which is consistent with what is shown in **(c)**.

The two notable observations made above, namely, the existence of finite $\text{VMM}_{1/2}$ in the gapless case and suppression of VMM near Dirac points in the gapped case, contradict the naïve picture of valley Chern number-based bulk-like behaviors. In both observations, the sign variation in valley field is right at the center of the phenomena. A clue is given below which connects the sign variation to the nontrivial role played by the asymmetric boundary condition of vanishing site amplitudes, e.g., $F_A(x = W/2) = F_B(x = -W/2) = 0$ [37]. As this condition effectively boosts up the on-site energy of A (B) site on the boundary $y = W/2$ ($-W/2$) to infinity, it introduces in the y -direction a *twist in on-site energy* and consequently in ‘ $\rho_A - \rho_B$ ’, too, resulting in antisymmetric or nearly antisymmetric valley fields. From the theoretical perspective, such twist implies a nontrivial alteration of valley physics by the boundaries. As will be shown in **Sec. IV-1** and **Appendix B**, as the result of boundary asymmetry, a pseudo vector potential parameter “ $A_x^{(BC)}(\tau)$ ” emerges and changes the valley field nontrivially.

Gapless zigzag graphene nanoribbon

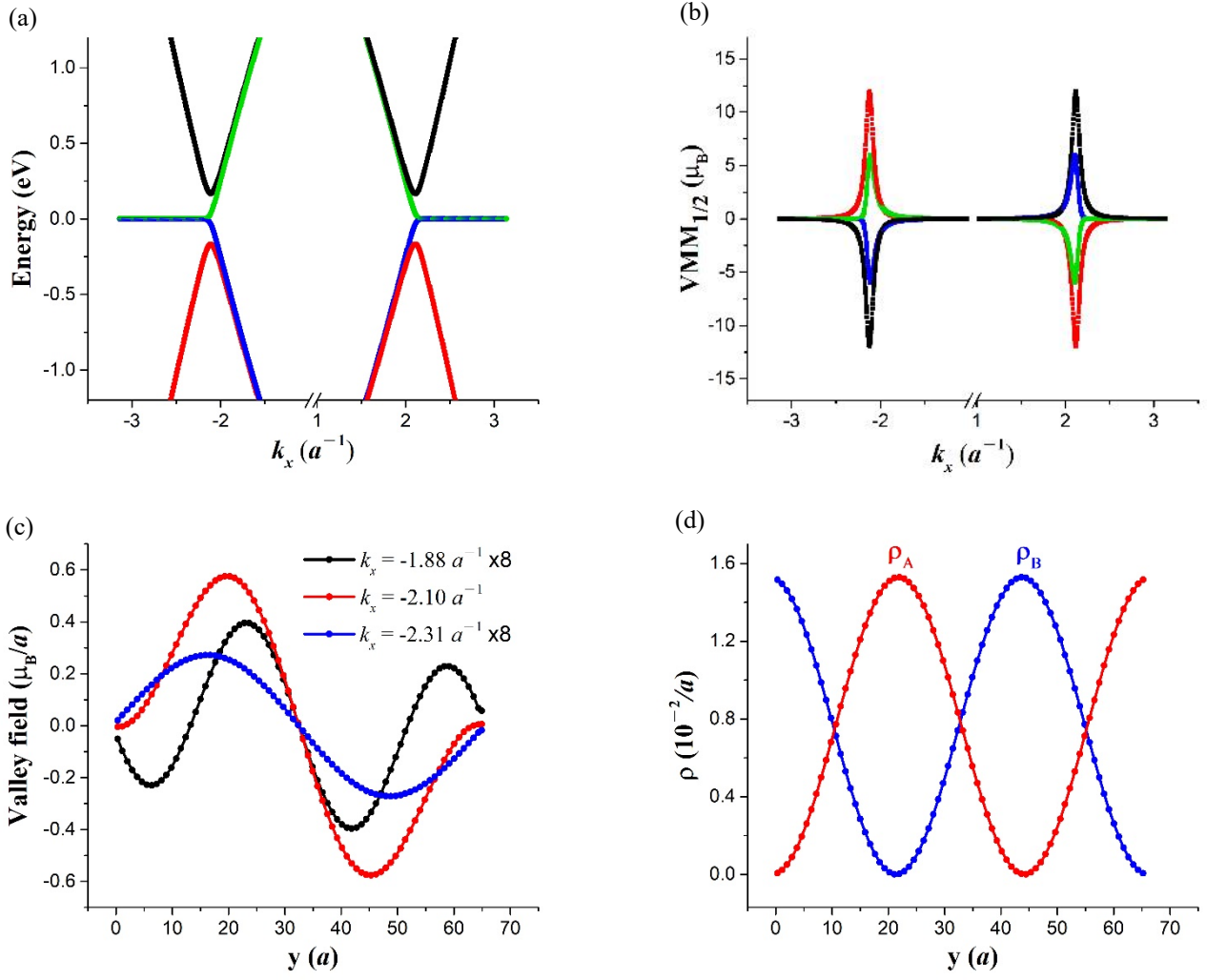
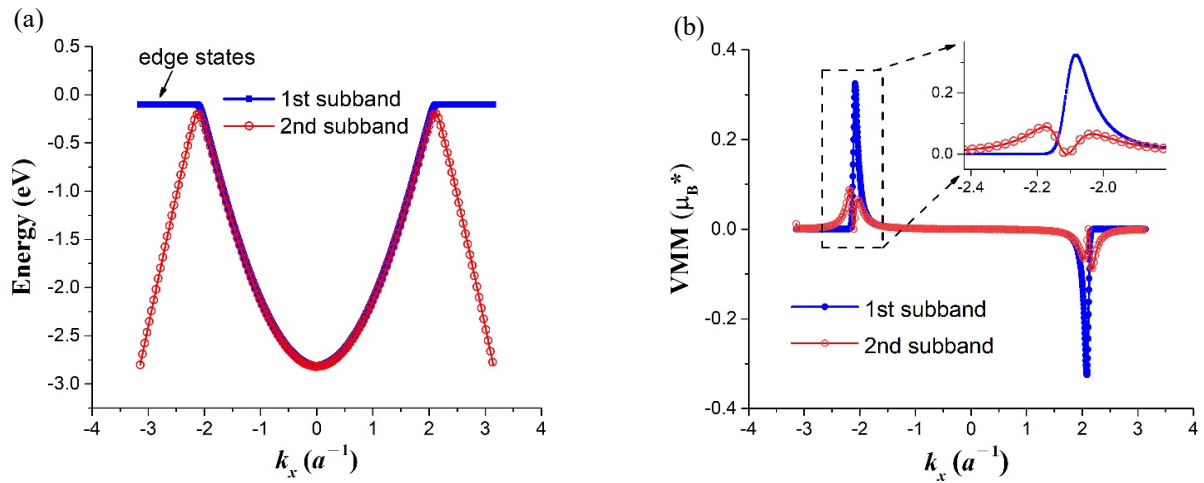


Figure 7. Vanishing valley magnetic moments (VMMs) but finite valley fields in gapless zigzag graphene nanoribbon (ZGNR) A gapless ($\Delta = 0$ eV) ZGNR with $W = 65.8a$ is considered. **(a)** Subbands. **(b)** Valley field accumulated over half width of the ribbon ($VMM_{1/2}$) vs. k_x for each subband. The color in **(a)** and **(b)** is used as band index. While VMM always vanishes independent of the state, $VMM_{1/2}$ can sometimes exceed $10 \mu_B$. **(c)** depicts nontrivial, antisymmetric valley fields of a few second subband states in the neighborhood of Dirac point ($k_x = -2.10 a^{-1}$). **(d)** shows $\rho_A(y)$ and $\rho_B(y)$ of the state at Dirac point in **(c)**. Overall, a sign oscillation exists in corresponding $\rho_{\text{diff}}(y) = \rho_A(y) - \rho_B(y)$ and valley field.

Gapped zigzag graphene nanoribbon



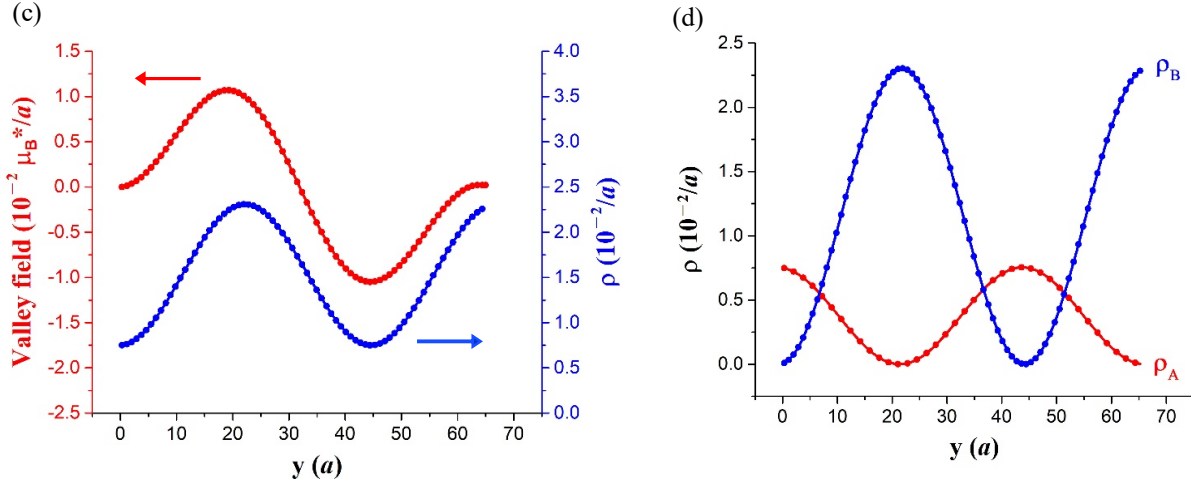


Figure 8. Valley magnetic moments (VMMs) and valley fields in gapped zigzag graphene nanoribbon (ZGNR) Gapped ZGNR with abrupt boundaries is considered, with width $W = 65.8 a$ and gap parameter $\Delta = 0.1 \text{ eV}$. **(a)** Top two valence subbands. **(b)** VMM vs k_x for bands in **(a)**, which reveals vanishing VMMs for edge states (flat part of blue curve in **(a)**), and an overall suppression of VMM near each Dirac point ($k_x = \pm 2.10 a^{-1}$), in the case of second valence subband. **(c)** presents valley field and $\rho(y)$ of the second subband state at Dirac point ($k_x = -2.10 a^{-1}$), with corresponding $\rho_A(y)$ and $\rho_B(y)$ shown in **(d)**.

iv) Graphene structures with gap inversion ($\Delta / -\Delta$) interfaces

Topological interface states exist between regions of distinct Chern numbers, and in graphene, too, when a $\Delta / -\Delta$ interface is present inducing a sign change in valley Chern number across the interface. [16–19]

We present valley fields in graphene nanoribbons with a center-aligned $\Delta / -\Delta$ interface running along the ribbon as depicted in **Figure 9**.

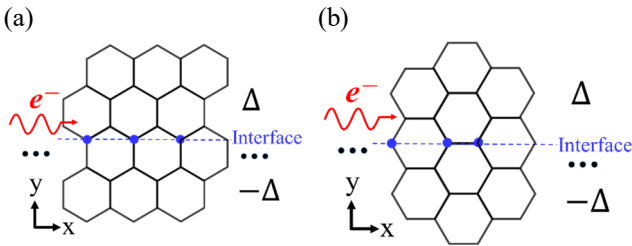


Figure 9. Structures with gap inversion interfaces (a) ZGNR (b) AGNR.

Figures 10 and 11 feature a zigzag graphene nanoribbon (ZGNR) and an armchair graphene nanoribbon (AGNR), respectively, both with the gap inversion interface, gap

parameter $\Delta = 1 \text{ eV}$, and ribbon width $w \approx 16 a$. In the two cases, the inversion results in topological interface states in and outside the bulk gap ($-1 \text{ eV}, 1 \text{ eV}$), turning the ZGNR gapless (in **Figure 10 (a)**) while the AGNR extremely narrow-gapped (in **Figure 11 (a)**).

In the zigzag case, **Figure 10** shows valley fields of three states. Two of them are interface states above (in **(b)**) and in (in **(c)**) the bulk gap, respectively, with field distributions concentrated near the interface. The third one is a non-interface state with field distribution repelled away from the interface (in **(d)**). They all show topology-induced sign flip across the interface.

In the armchair case, **Figure 11** shows valley fields of three states, again with two of them interface states above (in **(b)**) and in (in **(c)**) the bulk gap, respectively, and the third one a non-interface state (in **(d)**). The fields show a trend like that in the zigzag case with, however, a critical distinction – greatly suppressed amplitude with maximum magnitude $O(10^{-3} \mu_B^*/a)$ – $O(10^{-4} \mu_B^*/a)$ in the armchair case vs. sizable amplitude with maximum magnitude $O(10^{-2} \mu_B^*/a)$ in the zigzag case. The suppression derives from the valley mixing that results from the strong intervalley scattering located at the interface in the case of interface states and, additionally, at the abrupt terminating boundary in the case of non-interface states.

Zigzag graphene nanoribbon

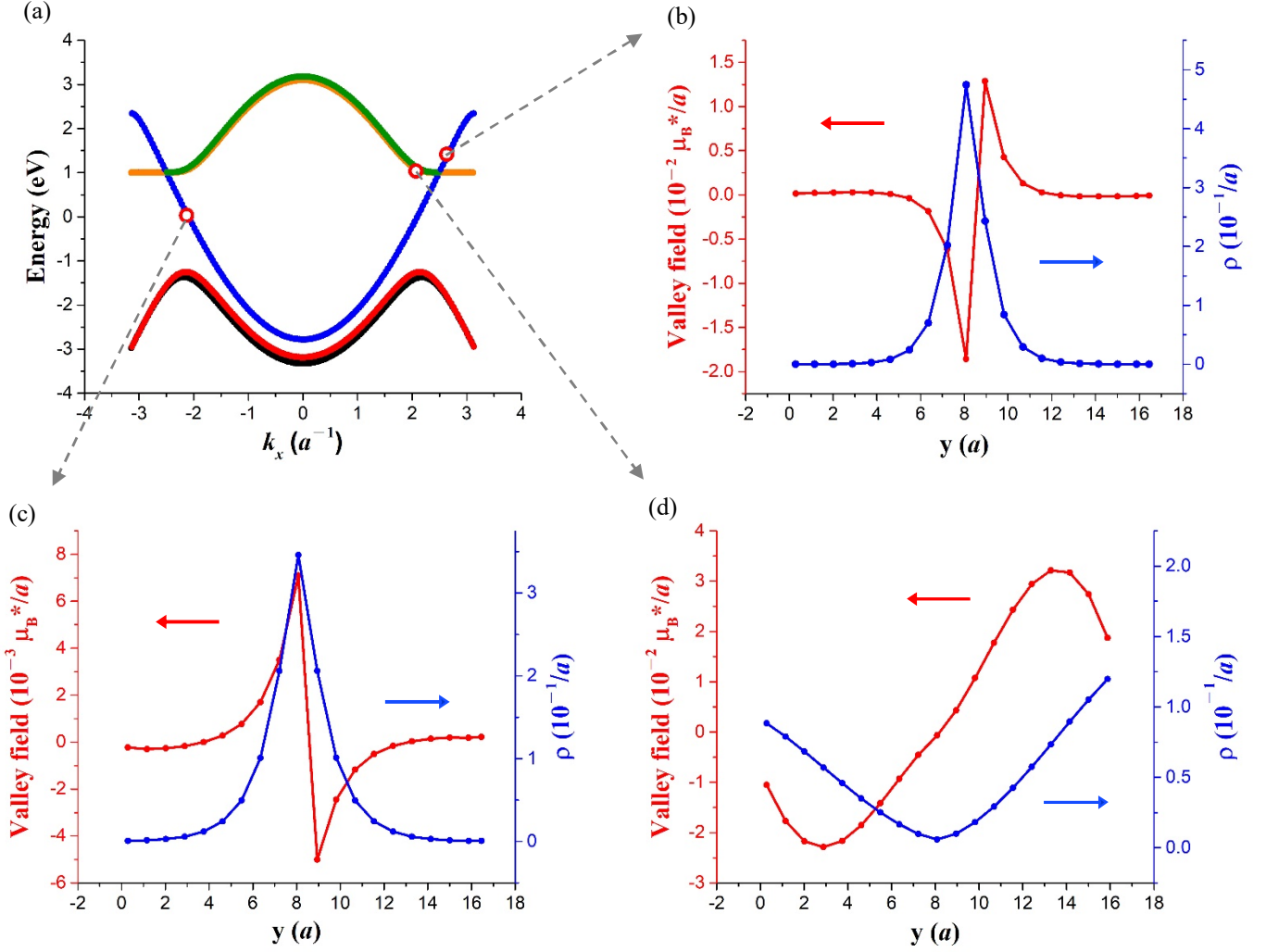


Figure 10. ZGNR with $\Delta / -\Delta$ interface The structure has ribbon width $W = 16.45 a$ and gap parameter $\Delta = 1$ eV. **(a)** Gapless subband structure, with topological interface state band (blue) existing in and outside the bulk gap (-1 eV, 1 eV). Such interface states are valley polarized and can provide topological 1D channels of valley currents, as experimentally observed in the bilayer graphene structure with AB / BA-stacking domain boundary [18]. **(b)** Valley field and probability distribution ($\rho(y)$) of an *above-bulk-gap* interface state ($k_x = 2.64 a^{-1}$). **(c)** Valley field and $\rho(y)$ of an *in-bulk-gap* interface state ($k_x = -2.10 a^{-1}$). The two interface states carry opposite valleys, so corresponding valley fields are reversed in sign. Both valley fields are confined to the interface, with sizable amplitudes reflecting strong valley polarization. **(d)** Valley field and $\rho(y)$ of a non-interface state ($k_x = 2.14 a^{-1}$), with distribution repelled away from the interface. Local signs of valley fields in **(b)-(d)** all flip across the interface in a way consistent with local valley Chern numbers. The result of interface states here is complementary to that of Louie et al. [56], where topological interface states are shown to exist between two end-to-end connected, gapless AGNRs characterized by different Z_2 invariants.

Armchair graphene nanoribbon

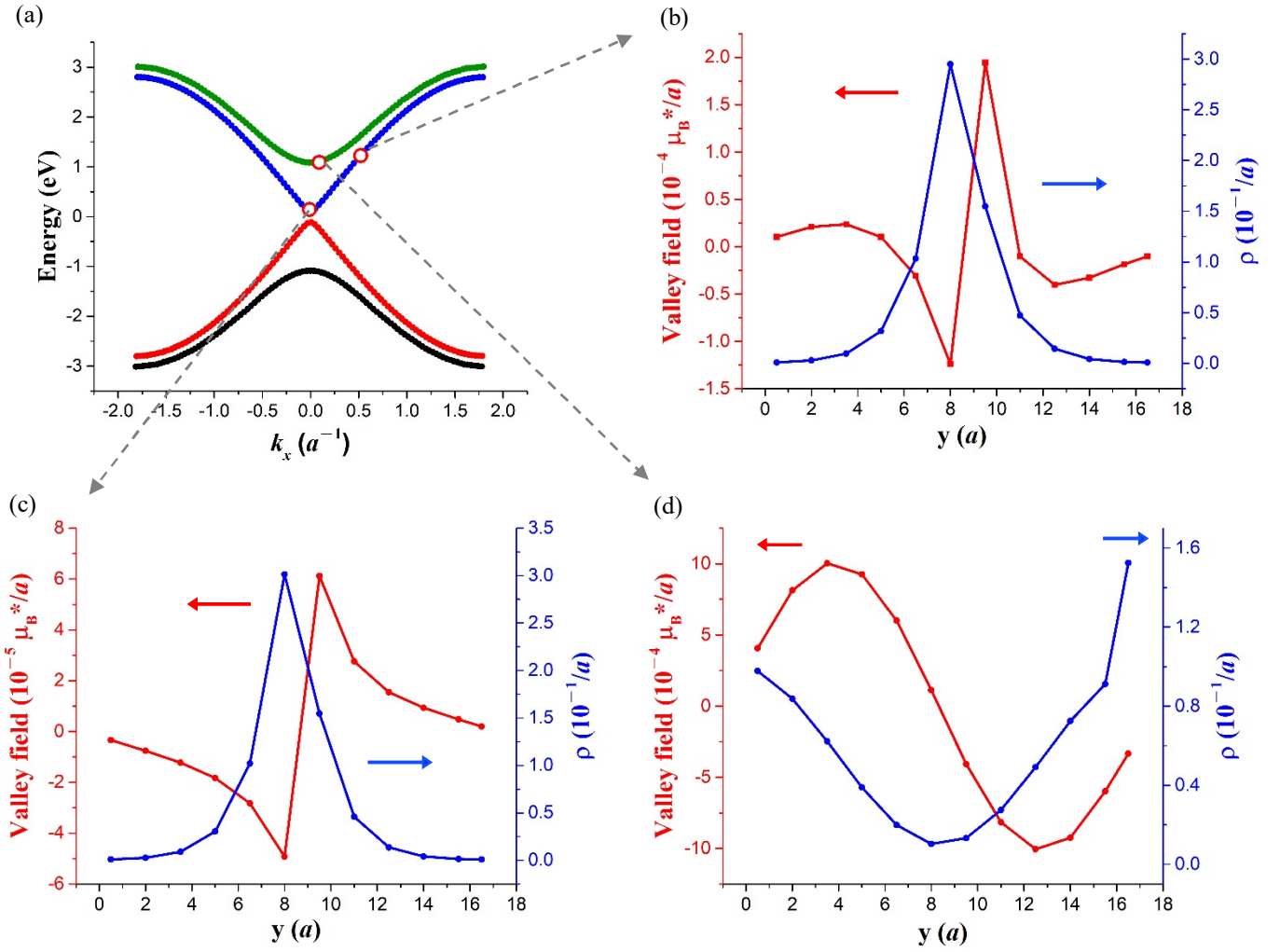


Figure 11. AGNR with $\Delta / -\Delta$ interface The structure has ribbon width $W = 16.5 a$ and gap parameter $\Delta = 1$ eV. **(a)** Narrow-gapped subband structure with interface state bands (red and blue) existing in and outside the bulk gap (-1 eV, 1 eV). Contrary to the ZGNR case, the gap here is finite, but approaches zero rapidly as Δ is reduced. It is a gap between symmetric and antisymmetric valley mixed states, with the mixing due to intervalley scattering near the interface. **(b)** Valley field and probability distribution ($\rho(y)$) of an *above-bulk-gap* interface state ($k_x = 0.51 a^{-1}$). **(c)** Valley field and $\rho(y)$ of an *in-bulk-gap* interface state ($k_x = 0.01 a^{-1}$). **(d)** Valley field and $\rho(y)$ of a non-interface state ($k_x = 0.073 a^{-1}$). Features of **(b)-(d)** are similar to those in the ZGNR case. However, the intervalley scattering induced valley mixing suppresses the valley polarization, resulting in the extremely small magnitude of valley field with maximum magnitude $O(10^{-3} \mu_B^*/a) - O(10^{-4} \mu_B^*/a)$ in **(b)-(d)**. The result of interface states here is complementary to that of Chou et al., where topological interface states are shown to exist between two end-to-end connected, gapless ZGNR-like structures characterized by different Z_2 invariants. [59]

v) Structures with valley mixing

When intervalley scattering exists, it mixes the opposite valley states and, thus, reduces the valley field magnitude.

Such scattering is present in graphene structures with armchair boundaries. In TMDC structures, because of spin-valley-orbital coupling, armchair edge scattering alone is not sufficient to couple valleys, unless a spin-flipping mechanism is simultaneously induced, for example, by a vertical electric field through the spin-orbit interaction. [74]

When intervalley coupling is present, the two valleys are evenly mixed giving a vanishing cell-orbital magnetic moment. A vertical magnetic field can be introduced to break the even mixing and polarize the state via the valley-Zeeman interaction, with the polarization dependent on the competition between the intervalley coupling and the valley-Zeeman interaction.

Graphene quantum dots

Figure 12 shows both valley fields and probability distributions ($\rho(x, y)$) of the top valence band energy level, in

two QDs formed with confinement barriers and subject to a uniform, valley-polarizing magnetic field B_z , with $\mu_B^* B_z = -2.35$ meV. The QDs have contrasting aspect ratios, with dimensions $W_x = 13.3 a < W_y = 19 a$ in **(a)**, and $W_x = 30.6 a > W_y = 9 a$ in **(b)**, giving varied armchair edge induced intervalley scattering / mixing and corresponding strong contrast between the two valley magnetic moments - $\mu_{\text{QD}} = 0.75 \mu_B^*$ in **(a)** and

$\mu_{\text{QD}} = 0.071 \mu_B^*$ in **(b)**. Since the intervalley scattering mainly occurs at the outer armchair edge, weaker (stronger) valley mixing exists in **(a)** (**(b)**), thus resulting in the magnitude contrast between **(a)** and **(b)** in μ_{QD} and valley field as well.

Graphene quantum dots

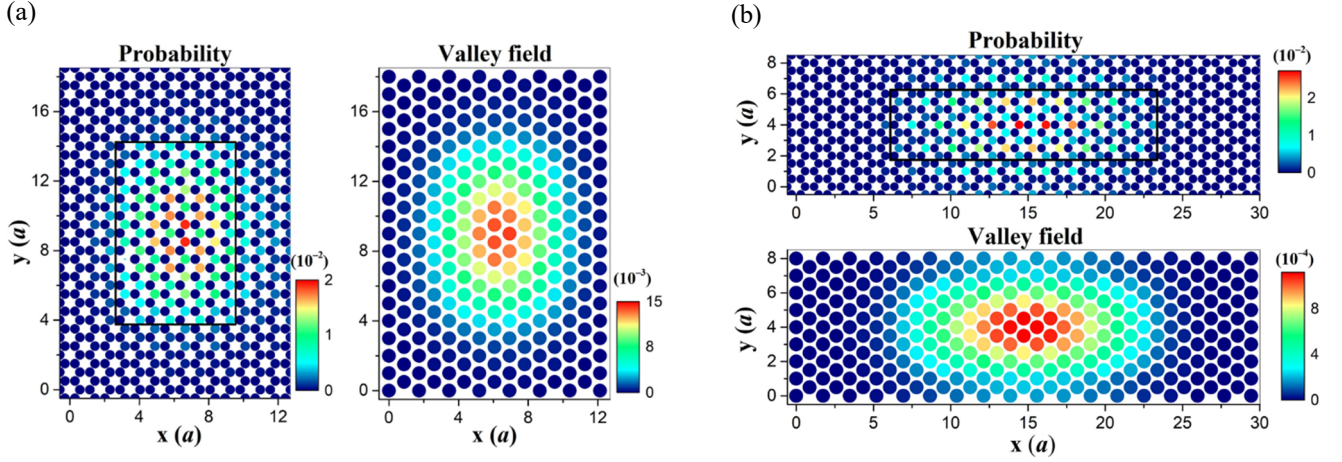


Figure 12. Magnetic field induced valley polarization in QDs Valley fields (in units of $\mu_B^*/(\text{hexagon area})$) and probability distributions ($\rho(x, y)$) in two QDs with dimensions $W_x = 13.3 a$ and $W_y = 19 a$ in **(a)** and $W_x = 30.6 a$ and $W_y = 9 a$ in **(b)**. The inner rectangular box in each graph indicates the quantum well region. Bulk gap parameters are given by $\Delta_{\text{well}} = 2$ eV in the well and $\Delta_{\text{barrier}} = 2.3$ eV outside the well. Electron energy $E = -2.15$ eV and the valley magnetic moment $\mu_{\text{QD}} = 0.75 \mu_B^*$ in **(a)**; $E = -2.16$ eV and $\mu_{\text{QD}} = 0.071 \mu_B^*$ in **(b)**. In both QDs, lack of reflection symmetry results in slightly asymmetric distributions of both $\rho(x, y)$ and valley field about the vertical center line. Since the intervalley scattering mainly occurs at the outer armchair edge, weaker (stronger) valley mixing exists in **(a)** (**(b)**), thus resulting in the magnitude contrast in both μ_{QD} and valley field between **(a)** and **(b)**.

Armchair graphene Q1D structures

A similar competition occurs between intervalley coupling and valley-Zeeman interaction, in an armchair graphene Q1D structure placed in valley-polarizing magnetic field. **Figure 13** presents valley fields of top two valence subbands in the armchair graphene nanoribbon with ribbon width $W = 19 a$. The polarizing magnetic field is given by $\mu_B^* B_z = -235$ meV. **(a)** shows the two subbands. **(b)** shows valley magnetic moment (VMM) vs. k_x for each subband. **(c)** and **(d)** present raw data of probability distribution ($\rho(y)$) and valley field, respectively, without coarse grain averaging, of the top

subband state at $k_x = -0.018 a^{-1}$.

With the abrupt armchair edges, a strong valley mixing is induced, which has several implications: i) it limits the valley field and valley magnetic moment as well, resulting in $|\mu_{\text{AGNR}}| < 0.02 \mu_B^*$ in the two subbands as shown in **(b)**; ii) it breaks the probability-valley field correlation, as can be verified by comparing **(c)** and **(d)**; and iii) it leads to the intervalley interference – rapid oscillations manifested in both $\rho(y)$ and valley field shown in **(c)** and **(d)**.

Armchair graphene nanoribbon

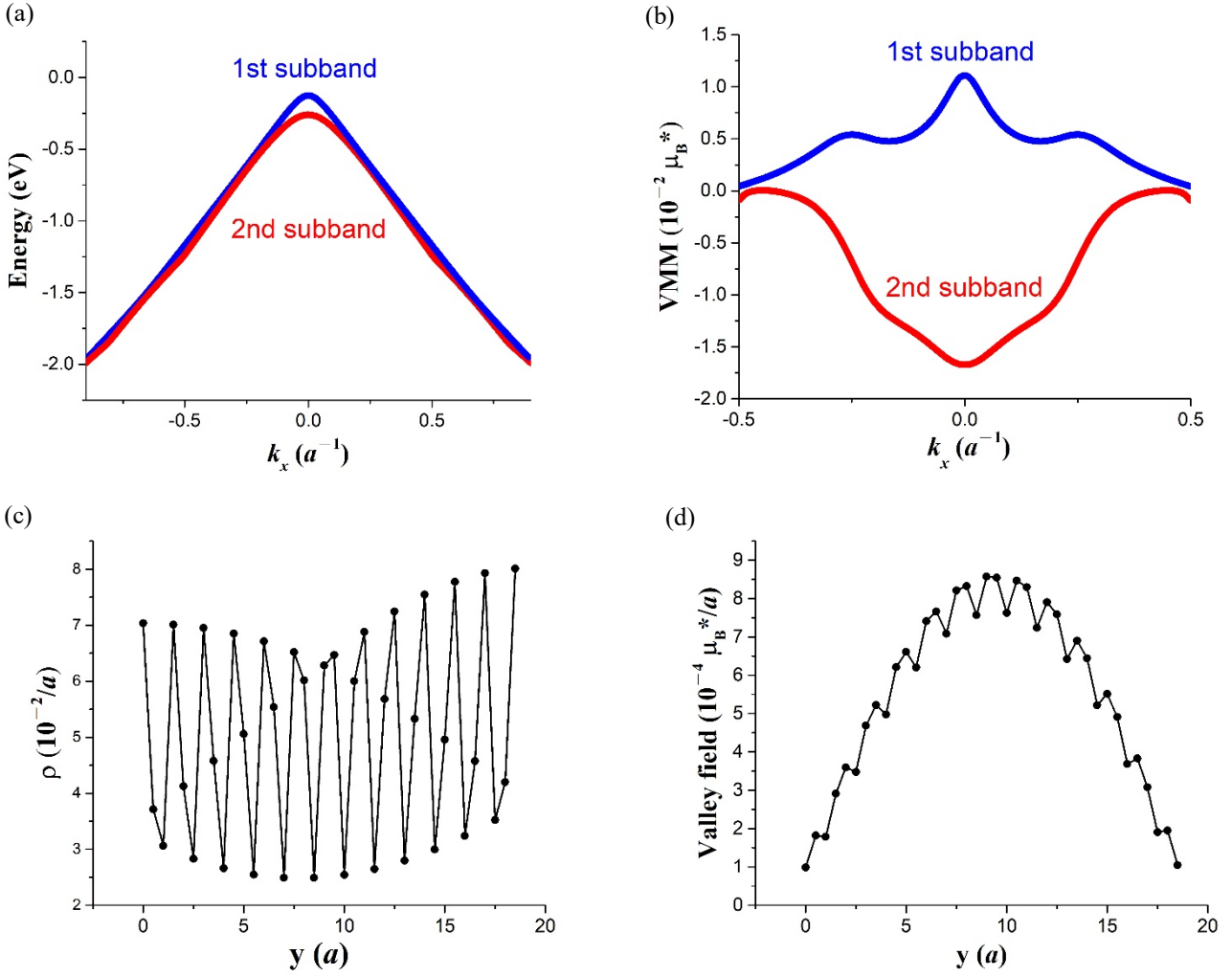


Figure 13. Magnetic field polarized valley field in AGNR The ribbon has ribbon width $W = 19 a$ and bulk gap parameter $\Delta = 0.02$ eV. (a) Top and second valence subbands. (b) Valley magnetic moment (VMM) vs k_x of the bands in (a). (c) and (d) are raw data of $\rho(y)$ and valley field, respectively, without coarse grain averaging, of the top subband state at $k_x = -0.018 a^{-1}$, both of which show rapid oscillations – the signature of valley mixing.

Armchair TMDC Q1D structures

Figure 14 features valley-unpolarized electron states at $k_x = -0.011 a^{-1}$ in two armchair WSe₂ Q1D structures, one of which has ribbon width $W = 25 a$ and is confined by abrupt edges (in (a)), and the other is confined by barriers with channel width $W_{\text{channel}} = 25 a$ and barrier width $W_{\text{barrier}} = 35 a$ (in (b)). Both structures are subject to a vertical electric field $E_z = 10$ mV/ a to effect intervalley scattering. Both valley fields and probability distributions are presented. As shown in the figure, the scattering results, in the two cases, quantitatively similar, antisymmetric valley fields with small amplitudes and corresponding vanishing valley magnetic moments, as well as breaking of probability-valley field

correlation. As for the antisymmetric feature shown in the valley field profile, the small amplitude implies its being some secondary effect in contrast to that observed in the ZGNR case in **Figures 7 and 8**. Without going into detailed explanation, we only briefly mention the weak valley asymmetry at a nonvanishing k_x as the cause for the feature. Such asymmetry results in slightly asymmetric, valley-contrasting profiles of $\rho_K(y)$ and $\rho_{K'}(y)$ ($\rho_\tau(y)$ = probability distribution for the valley- τ component of electron state), ending up with antisymmetric $\rho_K(y) - \rho_{K'}(y)$ and correspondingly antisymmetric valley field, too. On the other hand, the sum $\rho_K(y) + \rho_{K'}(y)$, i.e., $\rho(y)$ remains symmetric as shown in the figure.

Armchair WSe₂ Q1D structure

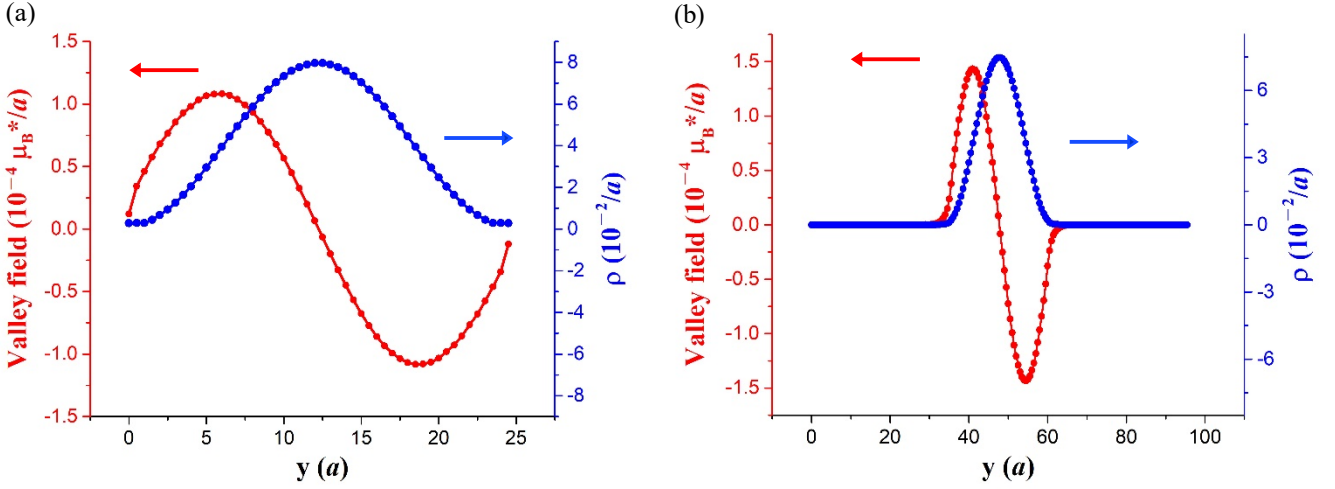


Figure 14. Unpolarized valley fields in armchair WSe₂ Q1D structures Valley fields and $\rho(y)$'s of unpolarized top valence subband states at $k_x = -0.011 a^{-1}$, in two armchair WSe₂ Q1D structures. The structure considered in (a) is confined by abrupt edges with ribbon width $W = 25 a$. The structure considered in (b) is confined by barriers with channel width $W_{\text{channel}} = 25 a$ and barrier width $W_{\text{barrier}} = 35 a$. Both structures are subject to a vertical electric field $E_z = 10 \text{ mV}/a$. In the case of barrier confinement, a negative on-site energy (-1 eV) is applied to form the barrier.

IV. Valley field mechanics: field equations and

local magnetic / electric field effects

Local valley phenomena can often be analytically studied for insights. For such studies, this section presents “valley field mechanics” centering on valley field equations and local field effects. The equations are briefly described. Based on the equations, effects of space-dependent external electric and magnetic fields are discussed, with important implications for local valley control via external fields.

A Ginzburg-Landau type field equation exists for the valley field (denoted m below). Depending on the approximations involved, the equation can be formulated in various analytic forms. Two relatively simple forms of the equation – one-band picture based *variant Schrodinger form* and two-band picture based *Klein-Gordon form* are illustrated in this work. As discussed in **Sec. III**, one-band picture implies relatively monotonous valley physics and is suitable for describing TMDC electron states. In graphene where A and B site orbitals respectively dominate conduction and valence band edge states, however, such a picture is primarily valid for low energy electrons near Dirac points, such as those in weakly, smoothly modulated structures. In the presence of sizable modulation, mixing of both orbitals or, equivalently, band edge states across the gap occurs. A suitable description in the case therefore requires the Dirac model, where both conduction and valence bands are included. Due to the correspondence between site orbitals and band edge states, such a description would be

valuable to the study of phenomena involving spatially varying ρ_A and ρ_B .

As valley fields vary with materials and structures, we select the following two cases for presentation, each with unique physics: i) ZGNRs, and ii) graphene Q1D structures confined with barriers, both of which are graphene-based and can potentially show versatile valley field behaviors. As such, **Sec. IV-1** is focused on discussing the *Klein-Gordon form* in the two cases, leaving a description of the relatively simple Schrodinger form to **Appendix A**. On the other hand, due to the novel, abrupt asymmetric boundary-induced valley behaviors shown in **Sec. III-2**, physics in ZGNRs is relatively complicated than that in graphene Q1D structures confined with barriers. External field effects are therefore discussed in the second case, for a relatively transparent illumination of the effects, in **Sec. IV-2**. **Sec. IV-3** remarks on the general nature of valley field mechanics to close the section. Mathematical details for **Secs. IV-1** and **IV-2** are provided in **Appendices B** and **C**.

We note that this section primarily addresses valley fields in the limit of vanishing intervalley coupling, e.g., those in zigzag Q1D structures. For QDs and armchair Q1D structures, boundary-induced intervalley scattering may be present, as shown earlier in **Sec. III-2**. Inclusion of the valley mixing is discussed in **Appendix D**, in the weak coupling regime based on a perturbation theory. Away from the regime, valley mixing starts to suppress m ending up with an insignificant residual value. Such cases occur in QDs and AGNRs with abrupt boundaries and are best studied by a numerical approach as illustrated earlier in **Sec. III-2**.

IV-1. The variant Klein-Gordon theory

The Klein-Gordon theory summarized below provides a Dirac two-band based description of valley fields in the absence of external fields.

ZGNRs – structures confined by abrupt asymmetric boundaries

For a start, abrupt asymmetric boundaries in ZGNRs have an important impact on valley fields. For example, as discussed in **Sec. III-2**, it can lead to valley fields with nearly antisymmetric profiles or, equivalently, the suppression of valley magnetic moments near Dirac points. From the theoretical perspective, the foregoing nontrivial manifestation imply a fundamental alteration of valley physics by the boundaries. As can be shown, a pseudo vector potential parameter “ $A_x^{(BC)}(\tau)$ ” emerges in the theory as the result of boundary asymmetry. We give a sketch below and leave the details to **Appendix B**.

The boundary effect is discussed in terms of the total current $\int j_x dy$. As shown in **Appendix B**, it consists of two components: $\int j_x dy = \left(\frac{k_x}{E}\right) - \left(\frac{A_x^{(BC)}(\tau)}{E}\right)$, with $A_x^{(BC)}(\tau) = -\frac{\tau}{2} [\rho_{diff}(W/2) - \rho_{diff}(-W/2)]$. The foregoing result brings out the important parameter $A_x^{(BC)}(\tau)$, with interesting properties noted below.

- i) $A_x^{(BC)}(\tau)$ has a sign dependent on the valley index τ .
- ii) The magnitude “ $|A_x^{(BC)}(\tau)|$ ” is essentially the difference between ρ_{diff} 's of the two boundaries. As such, it is a measure of the boundary asymmetry.
- iii) $A_x^{(BC)}(\tau)$ has the interpretation of a pseudo vector potential, as follows. The current $\int j_x dy$ with two components shown above complies with the standard form of a current given in the presence of a magnetic field. For example, “ k_x/E ” can be identified as the free current in the Dirac model (See Eqn. (4)) and “ $A_x^{(BC)}(\tau)/E$ ” the magnetic component with $A_x^{(BC)}(\tau)$ the corresponding vector potential of some fictitious magnetic field. Due to the presence of valley dependence in the sign, $A_x^{(BC)}(\tau)$ is a pseudo vector potential as opposed to a genuine one which is valley independent.

Figure 15 provides a numerical band structure result that supports the above interpretation. It plots the second conduction subband in ZGNRs at various ribbon width W 's, and shows that k_x of a subband edge state shifts away by “ τ/W ” from the Dirac point, in a valley contrasting fashion. This shift is consistent with the presence of a pseudo vector potential $A_x^{(BC)}(\tau)$. Such presence induces a corresponding change in the

Hamiltonian with the substitution $k_x \rightarrow k_x - A_x^{(BC)}(\tau)$ ($A_x^{(BC)}(\tau) = \tau/W$), and produces the observed wave vector shift. Due to the substitution, it places the band edge at $k_x = A_x^{(BC)}$ instead of the Dirac point ($k_x = 0$).

Since $A_x^{(BC)}(\tau)$ has a pseudo magnetic origin, it may very well contribute to the magnetization current distribution $\partial_y m(y)$. Indeed, as shown in **Appendix B**,

$\partial_y m(y) = \frac{\tau \partial_y \rho_{diff}}{2E} + \frac{A_x^{(BC)}}{E} \rho$. With the foregoing expression, the effect of asymmetric boundaries on valley field can be suitably accounted for.

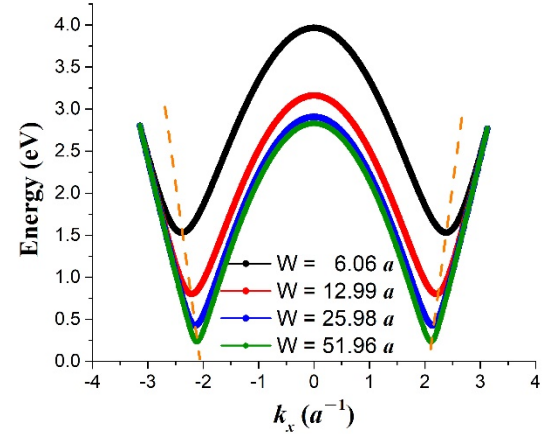


Figure 15. Abrupt asymmetric boundaries-induced Rashba shift and corresponding pseudo vector potential The second conduction band at various ribbon width W 's. The band edge moves away from Dirac point when W decreases. The ZGNR is characterized by bulk gap parameter $\Delta = 0.1 eV$.

Based on the foregoing analysis, we proceed to derive the corresponding valley field equation. As shown in **Appendix B**, in the case where bulk gap parameter $\Delta = \text{constant}$, we obtain

$$H_{KL} \partial_y^2 m(y) = E^2 \partial_y^2 m(y), \quad (15)$$

$$H_{KL} \equiv -\frac{1}{4} \partial_y^2 + k_x^2 + \Delta^2,$$

($H_{KL} \equiv$ corresponding Klein-Gordon operator) along with the following boundary condition involving $A_x^{(BC)}$:

$$m(\pm W/2) = 0,$$

$$\left[\pm k_x (k_x - A_x^{(BC)}) - E(\Delta \pm E) \right] \partial_y m(\pm W/2) \quad (16)$$

$$-\frac{1}{2} (k_x - A_x^{(BC)}) \partial_y^2 m(\pm W/2) = 0.$$

In the case of a subband edge state ($k_x = A_x^{(BC)}$), Eqns. (15) and (16) manifest mirror symmetry about the ZGNR center axis ($y = 0$) and imply a corresponding parity symmetry in $m(y)$.

In **Appendix B**, we further argue for the exact property of odd parity in $m(y)$ in the case of a subband edge state and, thus, the suppression of valley magnetic moments near Dirac points.

Graphene Q1D structures confined with barriers

We now turn to the case of graphene Q1D structures confined with barriers. In this case the effect of abrupt asymmetric boundaries is reduced and even negligible, in the limit of strong barrier confinement, where the barriers effectively block electrons from reaching the boundary and seeing the effect of asymmetry.

The structures considered are taken to be subject to a gap modulation $\Delta^{(y)}(y)$, with $\Delta^{(y)}(y)$ effecting a semi-infinite barrier confinement of electrons thus excluding the boundary asymmetry effect. We also ignore external fields. As shown in **Appendix C**, within the Dirac model it gives the following valley field equation:

$$H_{KL} m(y) = E^2 m(y),$$

$$H_{KL} \equiv -\frac{1}{4} \partial_y^2 m(y) + k_x^2 m(y) + \Delta^{(y)}(y) \int_{-\infty}^y \Delta^{(y)}(y) (\partial_y m) dy \quad (17)$$

along with the boundary condition

$$m(\pm\infty) = 0 \quad (18)$$

The theory expressed by Eqns. (17) and (18) excludes the presence of any electrical modulation other than $\Delta^{(y)}(y)$ or magnetic vector potential. Being external field-free, the theory serves as the zeroth-order description when studying effects of external fields.

IV-2. Effects of external fields

Effects of space-dependent electric and magnetic fields are discussed below, with focus on two aspects:

- i) *local valley-external field interactions*, for valley control via external fields;
- ii) *linear valley field response* to external fields.

An illustration is given in the case of graphene Q1D structures, which are taken to be subject to the electrical modulation $V^{(y)}(y)$ and / or magnetic vector potential $A_x(y)\hat{x}$.

Local valley-external field interaction

In the case of a homogeneous bulk in the presence of a uniform, out-of-plane magnetic field, e.g., B_z , the electron valley magnetic moment μ_{bulk} interacts with B_z showing the valley Zeeman energy “ $-B_z \mu_{bulk}$ ” [10, 27]. This fact has been exploited in **Sec. II-3** when introducing the generic definition of local magnetic moment m , using the generalized local expression “ $-B_z^{(probe)}(y)m(y)$ ” for the interaction between m

and the probing magnetic field $B_z^{(probe)}(y)$ both of which varies in space.

Similarly, in the presence of a uniform, in-plane, transverse electric field E_y , μ_{bulk} interacts with E_y showing the valley-orbit interaction energy “ $\frac{k_x}{\Delta_0} E_y \mu_{bulk}$ ” – a Rashba term in the electron energy [27]. This fact may also be exploited to define the local magnetic moment, for example, using the straightforward extension “ $\frac{k_x}{\Delta_0} E_y^{(probe)}(y)m(y)$ ” for the interaction between m and the probing electric field $E_y^{(probe)}(y)$ both of which vary in space.

More importantly, the above discussion leads to the expectation of existence of *local valley – external field interactions* in the forms given by the two foregoing generalized expressions. Such expectation is roughly borne out when we go through a rigorous discussion.

For the discussion, we consider the case of Q1D graphene structures confined with barriers. Let $m^{(0)}(y)$ and $E^{(0)}$ be the field-free valley field and electron state energy $E^{(0)}$, e.g., the solution to Eqns. (17) and (18) in the case. As shown in **Appendix C-3**, in the linear response regime, the corresponding local valley-external field interaction energy is given by

$$E_{\text{valley-field}} \approx \int_{-\infty}^{\infty} \frac{k_x}{E^{(0)}} \partial_y V^{(y)} m^{(0)}(y) dy - \int_{-\infty}^{\infty} B_z(y) m^{(0)}(y) dy \quad (19)$$

Eqn. (19) provides explicit, rigorous expressions of local valley-external field interactions. In particular, it gives

$$\frac{k_x}{E^{(0)}} \partial_y V^{(y)} m^{(0)}(y) \quad (20)$$

for the *local valley-orbit interaction* due to electric force (e.g., $-\partial_y V^{(y)}$), and

$$-B_z(y) m^{(0)}(y) \quad (21)$$

for the *local valley-Zeeman interaction* due to magnetic field $B_z(y)$. Such interactions serve as useful *mechanisms* for *local valley control* via space-dependent electric / magnetic fields.

Numerical examples are presented in **Figure 16** for local electric effects and **Figure 17** for local magnetic effects.

In **Figure 16**, a zigzag graphene nanoribbon with vanishing bulk gap is considered. It shows two contrasting

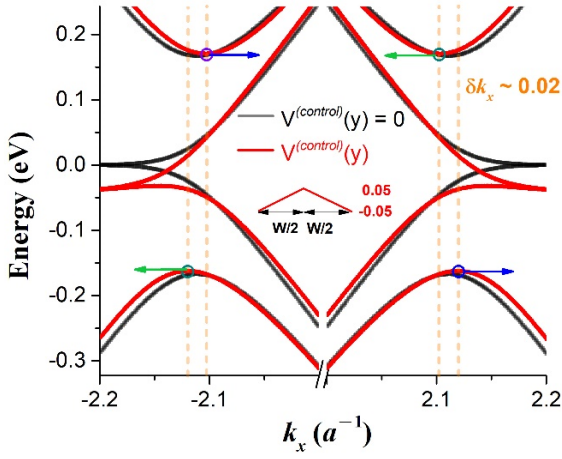


Figure 16. Local electric effects The same gapless graphene nanoribbon specified in **Figure 7** is considered. We refer to the gap between the second valence and second conduction subbands. Plotted in the graph are two contrasting subband structures – the black one with a direct gap when the structure is electric field free and the red one with an indirect gap when the structure is subject to a symmetric potential $V^{(control)}(y)$ which varies linearly between ± 0.05 eV. Due to the local valley-orbit interaction $V^{(control)}(y)$ induces band edge shifts in k_x , with opposite signs for the two valleys as well as for conduction and valence subbands, resulting in an indirect gap with $\delta k_x \sim 0.02$ a^{-1} (conduction-valence band edge wave vector difference).

subband structures – one with a direct gap when the structure is electric field free and the other with an indirect gap when the structure is subject to a symmetric potential $V^{(control)}(y)$. In order to appreciate the unique local electric effect induced by $V^{(control)}(y)$ here, we turn to a homogeneous bulk below.

Generally, in the bulk case, a simple linear, antisymmetric potential $V^{(control)}(y)$ would suffice to produce notable effects on energy bands. As the corresponding Rashba term “ $\frac{k_x}{\Delta_0} E_y \mu_{bulk}$ ” ($E_y = -\partial_y V^{(control)}$) in the case is linear in both k_x and τ , it would displace energy bands in a valley

contrasting way, resulting in the so called “valley Rashba splitting” of bands, useful for device applications [34]. However, in the case of gapless graphene ($\Delta = 0$), since μ_{bulk} vanishes, the splitting disappears, too.

On the other hand, in the ZGNR considered in **Figure 16**, despite $\Delta = 0$, the Rashba splitting is reinstated due to two local effects. Firstly, the field-free valley fields involved are antisymmetric but nonvanishing, as shown earlier in **Figure 7(c)**. Secondly, with $V^{(control)}(y)$ being symmetric, it results in a finite valley-orbit interaction energy integral $\int_{-\infty}^{\infty} \frac{k_x}{E^{(0)}} \partial_y V^{(control)} m^{(0)}(y) dy$. Indeed, as shown in **Figure 16**, finite, Rashba-type band edge shifts in k_x occur with opposite signs for the two valleys. Moreover, they occur with opposite signs too between conduction and valence subbands, resulting in an indirect gap with finite conduction-valence band edge wave vector difference $\delta k_x \sim 0.02$ a^{-1} . A similar gap alteration can be shown to occur in zigzag nanoribbons of gapped graphene, too.

We make a note in regard to the direct-indirect gap transformation illustrated. In view that the many-electron Hartree interaction may supply the required non-odd potential, it leads to the conjecture of zigzag graphene nanoribbons being intrinsically indirect-gapped.

Now we turn to **Figure 17**. **Figure 17(a)** shows the subbands when a *local* magnetic field (B_z) is applied to the lower half ribbon. While the involved valley fields are antisymmetric with vanishing sum totals, the total valley-Zeeman interaction energy due to B_z is finite, breaking valley degeneracy and leading to valley splitting. **Figure 17(b)** shows the subbands when a *uniform* magnetic field (B_z) is applied. The total valley-Zeeman interaction vanishes so B_z only introduces an energy shift due to the Landau orbital quantization, thus preserving the valley degeneracy.

Local magnetic effects

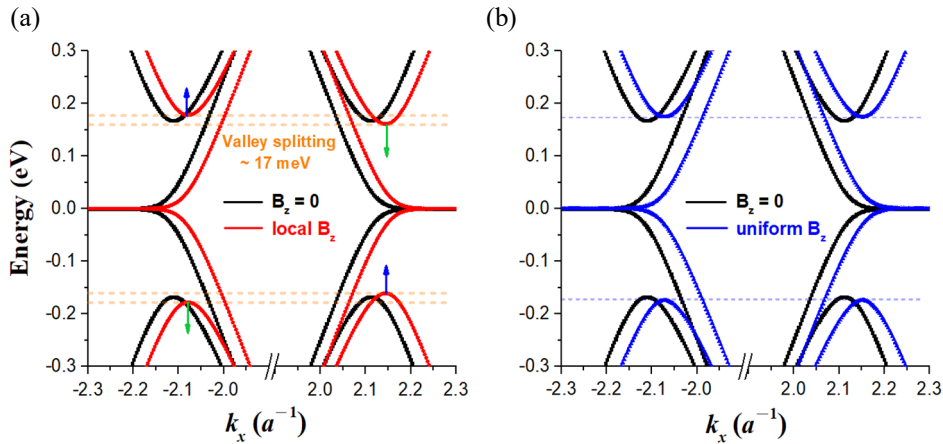


Figure 17. Local magnetic effects The same gapless graphene nanoribbon specified in **Figure 7** is considered. **(a)** The subbands when a *local* magnetic field (B_z) is applied to the lower half ribbon. It breaks valley degeneracy and leads to valley splitting. **(b)** The subbands when a *uniform* magnetic field (B_z) is applied. It only introduces an energy shift due to the Landau orbital quantization, thus preserving the valley degeneracy. $\mu_B B_z = 1$ meV is used in both **(a)** and **(b)**.

Overall, **Figures 16 and 17** send an important message – local valley physics expands flexibility and feasibility in both materials and valley control in valleytronics.

Local linear response: $m^{(1)}(y)$

We write $m(y) \approx m^{(0)}(y) + m^{(1)}(y)$ with $m^{(1)}(y)$ the linear response to external fields. As shown in **Appendix C-3**, a Klein-Gordon valley-field equation with a source term can be formulated for $m^{(1)}(y)$ in the linear response regime:

$$\left[H_{KL} - E^2 \right] m^{(1)}(y) = s^{(1)}(y; V^{(y)}, A_x), \quad (22)$$

where the source $s^{(1)}(y; V^{(y)}, A_x)$ is linear in the external fields as given in the Appendix.

Eqn. (22) is derived in the Appendix for the transverse field configuration, where an electric potential energy $V^{(y)}(y)$ and vector potential $A_x(y)$ are present. Such configuration is expected to have implications relevant to three-terminal device based valleytronic signal processing, where the ‘valley transconductance’ given by the ratio “ $m^{(1)}(y)$ / transverse field” would play an important device figure of merit.

IV-3. Nature of the mechanics

As a theoretical framework, valley field mechanics is featured by the following characteristics.

1) Intermediate-level quantum description

It provides a description of valley physics which interpolates between the global valley flavor and the primitive, site-resolved wave mechanics.

2) Space-dependent topological description

The observable ‘valley field’ transforms the \vec{k} -space, valley Chern number-based description to a \vec{r} -space one. It depicts the state symmetry distribution, including possible twists, in \vec{r} -space to suit a general, space-dependent situation. In the homogeneous bulk case, the valley field can be integrated to yield the valley magnetic moment and reflect the corresponding valley Chern number as well.

3) Normal mode mechanics

In the graphene case, an interpretation of ‘normal mode mechanics’ applies to the mechanics. In a sense, $\{ \rho_A - \rho_B, \rho_A + \rho_B \}$ form a set of ‘normal mode variables’ for the electronic motion, and offer, in comparison to the naive, site-

based variables $\{ \rho_A, \rho_B \}$, a relatively intuitive picture, with ‘ $\rho_A - \rho_B$ ’ describing the *intra-cell orbital motion* and ‘ $\rho_A + \rho_B$ ’ – the probability distribution as a function of cell position describing the global, *inter-cell translational motion*. The mechanics is focused on the ‘intra-cell normal mode’.

V. Conclusion and outlook

In conclusion, valleytronics in 2D materials is rooted in the existence of global valley flavor but extends far out to the rich dimension of local physics.

In order to explore the dimension, a Ginzburg-Landau order parameter type field – valley field has been introduced. The field is operationally defined in terms of local magnetic response, irrespective of electron state energy, and has the interpretation of local cell-orbital magnetic moment. From the theory standpoint, such a definition is not only free from the ambiguity issue, encountered in a valley flavor-based approach, of defining non-band-edge state’s valley flavor, but is also application-suited as it is directly linked to local valley-external field effects critical to the local valley control via space-dependent magnetic and electric fields.

The local physics can be addressed in the framework of valley field mechanics comprising valley field equations of variant Schrodinger or Klein-Gordon forms. The mechanics can be applied to the local linear response of valley fields. In particular, local valley-Zeeman and local valley-orbit-interaction effects, both valuable to local valley control, can be explored within the mechanics.

The study has revealed a spectrum of intriguing local valley phenomena, with quite a few profound twists with respect to valley flavor-based expectations and/or constraints, such as

- breaking of ‘valley flavor \leftrightarrow magnetic moment orientation’ correspondence,
- lifting of ‘inversion symmetry breaking’ condition for existence of magnetic moments,
- suppression or even elimination of valley magnetic moments, for near-Dirac point states in gapped graphene structures.

By revoking such constraints, it greatly expands the flexibility of valley control as well as the family of materials and structures suited to valleytronics. For example, *gapless, single-layer graphene* is now added to the family of graphene as a material for magnetic moment-based experiments or applications. This relaxes both the material and symmetry restrictions. Another example is given by the valley field sign flip in space shown in the study. It not only signifies the incompleteness of a global parameter – valley flavor or Chern number for capturing valley physics in general, but also has the following profound implication for flexible valley control, namely, in the case of a sign-varying valley field, *local*

magnetic fields of opposite signs, with signs correlating with those of local valley fields, may produce the same valley-Zeeman splitting and effect the same control via the local valley-Zeeman interaction.

In addition, non-valley applications may benefit from local valley physics, too, such as the direct-indirect gap control via an electric field.

The study also leads to additional insights into the material dependence of valleytronics - relatively versatile valley fields in graphene vs. relatively monotonous ones in TMDCs, apart from the well-known spin-valley locking contrast.

Last, the diverse local valley phenomena shown here suggest the attractive direction of valley field engineering - design and search for quantum structures to tailor valley fields via confinement, defects, boundaries, dopants, constituent materials — single- / multi- layer graphene (with [20–22,76] / without twists), single- / multi (homo or hetero)- layer transition metal dichalcogenides with parallel / antiparallel stackings (with / without twists) [25,26,46,47,77–80], etc. to suit applications.

Acknowledgement

We thank Prof. Mei-Yin Chou for various discussions, and Yen-Ju Lin for technical support in numerical calculations. We acknowledge the financial support of MoST, ROC through Contract No. MOST 109-2811-M-007-561. F.-W. C. acknowledges partial support from Academia Sinica.

Appendix A

The variant Schrodinger theory

We illustrate discuss the variant Schrodinger equation in the Q1D case. The discussion can easily be generalized to the quantum dot case.

The structure considered is subject to the modulation of $V_{total}^{(y)}(y)$, where

$$V_{total}^{(y)}(y) = \begin{cases} V^{(y)}(y) & \text{(TMDCs)} \\ V^{(y)}(y) \pm \delta\Delta^{(y)}(y) & \text{(graphene)} \end{cases} \quad (23)$$

with the inclusion of additional contribution $\delta\Delta^{(y)}(y)$ in the graphene case (+ / - for conduction / valence band; $\delta\Delta^{(y)}(y)$ = gap modulation in graphene).

The derivation is based on the effective-mass approximation,

$$\psi(x, y) = \exp(ik_x x) f(y) \phi_\tau(x, y) \quad (24)$$

($f(y)$ = slowly varying envelop function, $\phi_\tau(x, y)$ = band-edge Bloch state at valley τ). $f(y)$ satisfies the following

effective-mass equation:

$$\frac{1}{2m_{eff}} \left(k_x^2 - \partial_y^2 \right) f(y) + V_{total}^{(y)} f(y) = (E - E_{k=0}^-) f(y) \quad (25)$$

($E_{k=0}^-$ = corresponding bulk band edge).

Since $f(y)$ is real for a Q1D state, it follows that $\rho(y) = f(y)^2$, and

$$\widehat{H}_S \rho(y) = (E - E_{k=0}^-) \partial_y \rho(y), \quad (26)$$

$$\begin{aligned} \widehat{H}_S & \\ & \equiv \frac{1}{2m_{eff}} \left(k_x^2 - \frac{1}{4} \partial_y^2 \right) \partial_y + V_{total}^{(y)}(y) \partial_y + \frac{\partial_y V_{total}^{(y)}(y)}{2} \end{aligned}$$

Finally, using $m(y) \sim \rho(y) \mu_\tau$ (Eqn. (14)) in Eqn. (26), we obtain the Schrodinger equation for $m(y)$:

$$H_S m(y) = (E - E_{k=0}^-) \partial_y m(y) \quad (27)$$

To include $B_z(y)$ or the valley-orbit interaction, we make the following replacement in Eqn. (25) as shown in previous studies [27,74]:

$$\begin{aligned} V_{total}^{(y)}(y) & \rightarrow V_{total}^{(y)}(y) + V_{field}^{(y)}(y), \\ V_{field}^{(y)}(y) & = V_{valley-field}^{(y)}(y) + V_{non-valley-field}^{(y)}(y), \end{aligned} \quad (28)$$

$$V_{non-valley-field}^{(y)}(y) = -\frac{k_x - A_x(y)/2}{m_{eff}} A_x(y) - \mu_{other} B_z(y), \quad (29)$$

$$V_{valley-field}^{(y)}(y) = \begin{cases} \tau R_{VOI} k_x \partial_y V_{total}^{(y)} - \mu_\tau B_z(y) & \text{(TMDCs)} \\ \tau R_{VOI} k_x \left(\partial_y V_{total}^{(y)} - 2\partial_y \Delta \right) - \mu_\tau B_z(y) & \text{(graphene)} \end{cases} \quad (30)$$

(μ_τ = valley magnetic moment, μ_{other} = non-valley magnetic moment, R_{VOI} = valley-orbit interaction strength parameter). The same replacement in Eqn. (27) then gives the corresponding Schrodinger equation for $m(y)$ in the case.

Appendix B

The variant Klein-Gordon theory

in the presence of

abrupt asymmetric boundaries

Asymmetric boundaries have a nontrivial effect on the valley field. In particular, they induce a uniform, valley-dependent pseudo vector potential ($A_x^{(BC)}(\tau)$) and suppress

valley magnetic moments near the Dirac point, as numerically demonstrated in **Sec. III-2**. This Appendix uses zigzag graphene nanoribbons as the example, discusses the corresponding Klein-Gordon valley field equation in the absence of external fields, and illustrates the boundary effect analytically.

B-1 discusses the emergence of the vector potential. **B-2** derives the Klein-Gordon equation. **B-3** shows the suppression of valley magnetic moment near a Dirac point.

B-1. Emergence of the pseudo vector potential

For a start, in the absence of external fields, the Dirac equation leads to the following useful identities involving the current distribution j_x , probability distribution $\rho(y)$, and probability distribution difference $\rho_{diff}(y)$ (E = electron state energy, Δ = bulk gap parameter, and τ = valley index):

$$\partial_y j_x = 2\tau\Delta\rho - 2\tau E\rho_{diff}, \quad (31)$$

$$j_x = \frac{k_x}{E}\rho + \frac{\tau\partial_y\rho_{diff}}{2E}, \quad (32)$$

$$j_x = \frac{k_x}{\Delta}\rho_{diff} + \frac{\tau\partial_y\rho}{2\Delta}. \quad (33)$$

Effect of asymmetric boundaries

We examine the effect of asymmetric, vanishing amplitude boundary condition, e.g., $F_A(x=W/2) = F_B(x=-W/2) = 0$ in terms of the current distribution j_x .

Eqn. (32) gives

$$\int j_x dy = \frac{k_x - A_x^{(BC)}(\tau)}{E}, \quad (34)$$

$$A_x^{(BC)}(\tau) \equiv -\int \frac{\tau\partial_y\rho_{diff}}{2} dy = -\frac{\tau}{2}[\rho_{diff}(W/2) - \rho_{diff}(-W/2)]$$

Above, “ k_x/E ” is identical to the free current in Dirac model, and $A_x^{(BC)}(\tau)$ is identified as an asymmetric boundary-induced parameter. As $A_x^{(BC)}(\tau) \propto [\rho_{diff}(W/2) - \rho_{diff}(-W/2)]$, it serves as a measure of the boundary asymmetry. Moreover, based on the boundary condition of vanishing amplitudes, $\rho_{diff}(W/2) - \rho_{diff}(-W/2) = -[\rho_B(W/2) + \rho_A(-W/2)] \neq 0$ showing the existence of a finite $A_x^{(BC)}$.

According to Eqn. (34), the subband edge, where $\int j_x dy = 0$, occurs at $k_x = A_x^{(BC)}(\tau)$, implying a valley-dependent wave vector shift of the edge away from the Dirac point ($k_x = 0$). Such a shift suggests the substitution $k_x \rightarrow k_x - A_x^{(BC)}(\tau)$ with $A_x^{(BC)}(\tau)$ interpreted as a pseudo

vector potential parameter. A variational argument can be applied to obtain the parameter explicitly in terms of the ribbon width W . Without going through details of the argument, we provide the expression below:

$$A_x^{(BC)}(\tau) = -\tau \langle \rho_A + \rho_B \rangle_{average} = -\frac{\tau}{W} \quad (35)$$

($\langle \dots \rangle_{average}$ denotes the spatial average of the expression in bracket) in the case of non-edge states.

B-2. The Klein-Gordon equation

Apart from shifting the subband edge, the pseudo vector potential $A_x^{(BC)}(\tau)$ has a nontrivial effect on the valley field $m(y)$ as shown below. Combining Eqns. (7) and (34) gives the following magnetization current distribution

$$\partial_y m(y) = \frac{\tau\partial_y\rho_{diff}}{2E} + \frac{A_x^{(BC)}}{E}\rho, \quad (36)$$

where the second term on the right hand side explicitly shows the induction of a magnetization current by $A_x^{(BC)}(\tau)$. Such effect needs to be accounted for when deriving the valley field equation.

The equation

Eqns. (31)-(33) and (36) constitute a set of simultaneous equations for the four field variables $m(y)$, $j_x(y)$, $\rho_{diff}(y)$, and $\rho(y)$. Elimination of variables leads to the following equation for $m(y)$:

$$-\frac{1}{4}\partial_y^2 [\partial_y^2 m(y)] + (k_x^2 + \Delta^2) [\partial_y^2 m(y)] = E^2 [\partial_y^2 m(y)]. \quad (37)$$

Boundary conditions

The foregoing valley field equation is fourth order and so requires four boundary conditions. These conditions follow from the requirement of vanishing $m(y)$ and $j_x(y)$ at $y = \pm W/2$. Again, Eqns. (31)-(33) and (36) can be applied to convert these conditions into the following ones in terms of m and its derivative:

$$m(\pm W/2) = 0 \quad (38)$$

$$\begin{aligned} & [\pm k_x (k_x - A_x^{(BC)}) - E(\Delta \pm E)] \partial_y m(\pm W/2) \\ & - \frac{1}{2} (k_x - A_x^{(BC)}) \partial_y^2 m(\pm W/2) = 0. \end{aligned} \quad (39)$$

Eqns. (37)-(39) constitute the Klein-Gordon theory of valley fields in ZGNRs.

B-3. Parity of valley fields

Last, $m(y)$ of a subband edge state, where $k_x = A_x^{(BC)}$, is considered and shown to have an odd parity.

Proof:

- i) When $k_x = A_x^{(BC)}$, the valley field equation (37) and boundary conditions (38) and (39) are all mirror symmetric with respect to the reflection $y \leftrightarrow -y$. So the solution $m(y)$ has a parity symmetry.
- ii) Eqns. (31) – (33) and (36) can be used to show the following inequality

$$\begin{aligned} & \partial_y^2 m(W/2) - \partial_y^2 m(-W/2) \\ &= \frac{4}{E} (\Delta^2 - E^2) A_x^{(BC)} \\ &\neq 0 \end{aligned} \quad (40)$$

We thus conclude that $m(y)$ is odd.

Q.E.D.

As valley magnetic moments are sum totals of valley fields in space, the foregoing result implies the suppression of valley magnetic moments near Dirac points, in ZGNRs.

Appendix C

The variant Klein-Gordon theory

in the presence of space-dependent fields

This Appendix illustrates the mathematical development of valley field mechanics in space-dependent electric and magnetic fields, in the Dirac two-band model using Q1D graphene structures confined with barriers as the example. The field-free, Klein-Gordon theory is presented firstly, followed by an inclusion of external fields in the theory and the discussion of local valley-external field interactions, in the linear response regime.

Important connections exist among the valley field $m(y)$, current distribution $j_x(y)$, probability distribution $\rho(y)$, and probability distribution difference $\rho_{diff}(y)$, as expressed in Eqns. (7) and (8). The Appendix follows the strategy of taking $\rho_{diff}(y)$ as the auxiliary field, building the corresponding auxiliary field equation, and based on it, developing the valley field equation.

C-1 formulates the auxiliary field equation in the presence of external fields. **C-2** presents the field-free, Klein-Gordon valley field theory. **C-3** discusses the valley field theory in the presence of external fields as well as local valley-external field interactions, in the linear response regime.

C-1. The auxiliary field equation

For a start, we list below important identities including Eqns. (7) and (8), which involve $m(y)$, $j_x(y)$, $\rho_{diff}(y)$, and $\rho(y)$ and can be derived from the Dirac equation in the presence of external fields (E = electron state energy, $V^{(y)}$ = electrical potential energy, $A_x^{(y)}$ = vector potential, $\Delta^{(y)}$ = modulated gap, τ = valley index):

$$\begin{aligned} \partial_y j_x(y) &= 2\tau \Delta^{(y)}(y) \rho(y) - 2\tau [E - V^{(y)}(y)] \rho_{diff}(y), \\ j_x(y) &= \left(\frac{k_x - A_x(y)}{E - V^{(y)}(y)} \right) \rho(y) + \left(\frac{\tau}{2[E - V^{(y)}(y)]} \right) \partial_y \rho_{diff}(y), \\ j_x(y) &= \left(\frac{k_x - A_x(y)}{\Delta^{(y)}(y)} \right) \rho_{diff}(y) + \left(\frac{\tau}{2\Delta^{(y)}(y)} \right) \partial_y \rho(y), \\ \partial_y m(y) &= j_x(y) - \left[\int \langle j_x \rangle dy \right] \rho(y). \end{aligned} \quad (41)$$

Above identities constitute a set of simultaneous equations for $m(y)$, $j_x(y)$, $\rho_{diff}(y)$, and $\rho(y)$. Elimination of variables is applied, giving

$$0 = \left[-h_0 \partial_y \circ \hat{h}_2 + (\partial_y h_0) \hat{h}_2 + h_0 \hat{h}_1 \right] \rho_{diff}(y), \quad (42)$$

where h_0 , h_1 , and h_2 are operators defined below:

$$\begin{aligned} & h_0(V^{(y)}, A_x, E) \\ & \equiv 1 - \frac{\tau}{2\Delta^{(y)}} d_y \left[\frac{(k_x - A_x)}{E - V^{(y)}} \right] - \left[\frac{(k_x - A_x)}{E - V^{(y)}} \right]^2, \\ & \hat{h}_1(V^{(y)}, A_x, E) \rho_{diff} \\ & \equiv d_y \left[\frac{(k_x - A_x)}{E - V^{(y)}} \right] \frac{(k_x - A_x)}{\Delta^{(y)}} \rho_{diff} \\ & + \left[2\tau \Delta^{(y)} - \frac{d_y (k_x - A_x)}{E - V^{(y)}} \right] \frac{\tau}{2(E - V^{(y)})} d_y \rho_{diff}, \\ & + \frac{\tau (k_x - A_x)}{2(E - V^{(y)})^2} d_y^2 \rho_{diff} \\ & \hat{h}_2(V^{(y)}, A_x, E) \rho_{diff} \\ & \equiv \left[\frac{E - V^{(y)}}{\Delta^{(y)}} - \frac{(k_x - A_x)^2}{\Delta^{(y)}(E - V^{(y)})} \right] \rho_{diff} \\ & + \left[\frac{1}{4\Delta^{(y)}} d_y \left(\frac{1}{E - V^{(y)}} \right) + \frac{\tau (k_x - A_x)}{2(E - V^{(y)})^2} \right] d_y \rho_{diff} \\ & + \frac{1}{4\Delta^{(y)}(E - V^{(y)})} d_y^2 \rho_{diff} \end{aligned} \quad (43)$$

For graphene Q1D structures confined with barriers, we have the following boundary condition:

$$\rho_{diff}(y \rightarrow \pm\infty) \rightarrow 0. \quad (44)$$

Eqns. (42) and (44) constitute the auxiliary field equation in the presence of external fields.

C-2. Field-free Klein-Gordon theory

In the absence of external fields, we write

$$\begin{aligned}\rho(y) &\approx \rho^{(0)}(y), \\ \rho_{diff}(y) &= \rho_{diff}^{(0)}(y), \\ j_x(y) &= j_x^{(0)}(y), \\ m(y) &= m^{(0)}(y), \\ E &= E^{(0)}.\end{aligned}\quad (45)$$

Eqn. (41) can be applied to express $\rho_{diff}^{(0)}$, $\rho^{(0)}$, and $j_x^{(0)}(y)$ in terms of $E^{(0)}$ and $m^{(0)}(y)$:

$$\begin{aligned}\rho_{diff}^{(0)}[m^{(0)}] &= 2\tau E^{(0)} m^{(0)}(y), \\ \rho^{(0)}[m^{(0)}] &= 2\tau E^{(0)} \left[\hat{h}_0^{-1} \hat{h}_z \right]^{(0)} m^{(0)}(y) \\ &= \frac{2\tau E^{(0)2}}{\Delta^{(y)}(y)} m^{(0)}(y) + \frac{k_x}{E^{(0)}} \partial_y m^{(0)}(y) \\ &\quad + \frac{\tau}{2\Delta^{(y)}(y)} \partial_y^2 m^{(0)}(y),\end{aligned}\quad (46)$$

$$j_x^{(0)}[m^{(0)}] = \frac{k_x}{E^{(0)}} \rho^{(0)}[m^{(0)}] + \partial_y m^{(0)}(y)$$

$$([\dots]^{(0)} \equiv [\dots]_{|V^{(y)}=0, A_x=0, E=E^{(0)}}).$$

Expressions provided above are useful in deriving the valley field equation below and in the discussion of field effects in C-3.

Combining the expression of $\rho_{diff}^{(0)}[m^{(0)}]$ provided above and Eqns. (42) and (44) leads to the following valley field equation:

$$\begin{aligned}H_{KL} m^{(0)}(y) &= E_0^2 m^{(0)}(y), \\ H_{KL} m^{(0)}(y) &\equiv \left(k_x^2 - \frac{1}{4} \partial_y^2 \right) m^{(0)}(y) + \Delta^{(y)}(y) \int_{-\infty}^y \Delta^{(y)}(y) (\partial_y m^{(0)}(y)) dy', \\ m^{(0)}(y \rightarrow \pm\infty) &\rightarrow 0,\end{aligned}\quad (47)$$

with H_{KL} the field-free Klein-Gordon operator.

C-3. Effects of external fields

In the presence of $V^{(y)}$ or A_x , we derive the field effects in the linear response regime as follows. We linearize all relevant variables, e.g.,

$$\begin{aligned}\rho(y) &\approx \rho^{(0)}(y) + \rho^{(1)}(y), \\ \rho_{diff}(y) &\approx \rho_{diff}^{(0)}(y) + \rho_{diff}^{(1)}(y), \\ j_x(y) &\approx j_x^{(0)}(y) + j_x^{(1)}(y), \\ E &\approx E^{(0)} + E^{(1)}, \\ m(y) &\approx m^{(0)}(y) + m^{(1)}(y),\end{aligned}\quad (48)$$

where $\rho^{(1)}$, $\rho_{diff}^{(1)}$, $j_x^{(1)}$, $E^{(1)}$, and $m^{(1)}$ are field-induced responses linear in the fields. In particular, $E^{(1)}$ is given by the following first-order perturbation-theoretic expression in terms of the field-free solution:

$$\begin{aligned}E^{(1)} &= \langle V^{(y)} \rangle_0 - \langle A_x \rangle_0, \\ \langle V^{(y)} \rangle_0 &\equiv \int_{-\infty}^{\infty} V^{(y)}(y) \rho^{(0)}(y) dy, \\ \langle A_x \rangle_0 &\equiv \int_{-\infty}^{\infty} A_x(y) j_x^{(0)}(y) dy\end{aligned}\quad (49)$$

($\langle \dots \rangle_0$ denotes expectation value with respect to the field-free solution).

Local valley-orbit and valley-Zeeman interactions

Substituting the expressions provided in Eqn. (46) into Eqn. (49) and collecting the contributions to $\langle V^{(y)} \rangle_0$ and $\langle A_x \rangle_0$ from the valley-dependent terms, we obtain the following leading-order local valley-external field interaction energy

$$\begin{aligned}E_{\text{valley-field}} &\approx \int_{-\infty}^{\infty} \frac{k_x}{E^{(0)}} \partial_y V^{(y)} m^{(0)}(y) dy - \int_{-\infty}^{\infty} B_z(y) m^{(0)}(y) dy\end{aligned}\quad (50)$$

giving

$$\frac{k_x}{E^{(0)}} \partial_y V^{(y)} m^{(0)}(y)\quad (51)$$

as the *local valley-orbit interaction* and

$$-B_z(y) m^{(0)}(y)\quad (52)$$

as the *local valley-Zeeman interaction*.

Theory in the linear response regime

In the linear response regime, the field equation for $m^{(1)}(y)$ can be obtained by linearizing Eqns. (41) and (42), which yields the following Klein-Gordon equation with a source term:

$$[H_{KL} - E^2] m^{(1)}(y) = s^{(1)}(y; V^{(y)}, A_x).\quad (53)$$

This equation can be solved to provide $m^{(1)}(y)$ in terms of the external fields. Above, the source term $s^{(1)}(y; V^{(y)}, A_x)$ is an expression linear in $V^{(y)}$ and A_x , given below in terms of the field-free solution:

$$\begin{aligned}
s^{(1)}(y; V^{(y)}, A_x) & \\
&\equiv \frac{\tau}{2} \Delta^{(y)}(y) \int_{-\infty}^y \left[-\partial_y \circ \hat{h}_2 + \hat{h}_1 \right]^{(0)} d^{(1)}(y; V^{(y)}, A_x) dy, \\
& - \frac{\tau}{2} \Delta^{(y)}(y) \int_{-\infty}^y \frac{1}{[h_0]^{(0)}} \left[-h_0 \partial_y \circ \hat{h}_2 + (\partial_y h_0) \hat{h}_2 + h_0 \hat{h}_1 \right]^{(1)} m^{(0)}(y) dy \\
d^{(1)}(y; V^{(y)}, A_x) & \\
&\equiv \frac{1}{E_0} \int_{-\infty}^y \left[n_v^{(1)}(y) + n_{A_x}^{(1)}(y) \right] dy, \\
n_v^{(1)}(y) & \\
&\equiv V^{(y)}(y) \partial_y m_0(y) \\
& + \left\{ \frac{k_x [V^{(y)}(y) - \langle V^{(y)} \rangle_0]}{E_0} - \int_{-\infty}^y (\partial_y m_0) V^{(y)}(y) dy \right\} \rho_0(y) \\
n_{A_x}^{(1)}(y) &\equiv \left[\langle A_x \rangle_0 - A_x(y) \right] \rho_0(y)
\end{aligned} \tag{54}$$

($\langle A_x \rangle_0 \equiv \int_{-\infty}^{\infty} A_x(y) \rho_0(y) dy$; $[\dots]^{(0)}$ and $[\dots]^{(1)}$ denote the field-independent and linear-in-field parts of the expression in bracket, respectively).

Appendix D

Valley mixing

Intervalley K-K' scattering may occur in some quantum structures, such as those with interfaces running in the armchair direction in the case of graphene ones. In TMDC structures with such interfaces, because of spin-valley locking, the scattering can occur only when certain spin-flip mechanism is additional enabled, for example, by vertical electric or in-plane magnetic fields. [74] In either material, when intervalley scattering is present, the theory of valley fields must address the effect of valley mixing.

Below, we consider the weak intervalley coupling limit where

$$E_{\text{intervalley coupling}} \ll E_{\text{quantization}} \tag{55}$$

($E_{\text{intervalley coupling}}$ = intervalley coupling, $E_{\text{quantization}}$ = quantization energy), in Q1D TMDC and graphene structures confined with barriers.

Valley-degenerate case

Let $B_z(y) = 0$. Ignore the intervalley coupling first and focus on the zeroth-order solution - $m_{K(K')}^{(0)}(y)$ for K(K') valley field. The fields are governed by the Schrodinger Eqn. (27) or Klein-Gordon Eqn. (47), with corresponding energy $E_{K(K')}^{(0)}$. Due to the time reversal symmetry, $E_K^{(0)} = E_{K'}^{(0)}$ and $m_{K'}^{(0)}(y) = -m_K^{(0)}(y)$. Intervalley coupling mixes the two fields evenly, giving

$$m(y) = 0. \tag{56}$$

The result is valid when higher-order effects, e.g., valley-orbit interaction or trigonal band warping around a Dirac point are neglected. When they are included, a small yet finite difference exists between $|m_K^{(0)}(y)|$ and $|m_{K'}^{(0)}(y)|$ giving a residual $m(y)$, as shown in **Figure 14** with a full tight-binding calculation.

Valley-polarized case

A vertical magnetic field $B_z(y)$ can be applied to lift the degeneracy and polarize the state. Consider $B_z(y)$ in the linear regime. Described below is a one-parameter ($E_{\text{intervalley coupling}}$), two-state perturbation theory of the linear response $m^{(1)}(y)$.

In the Hilbert space of the two field-free, degenerate solutions, the two-state Hamiltonian is given by

$$H_{\text{armchair}} \approx \begin{pmatrix} E_{\text{valley-Zeeman}} & E_{\text{intervalley coupling}} \\ E_{\text{intervalley coupling}} & -E_{\text{valley-Zeeman}} \end{pmatrix} \tag{57}$$

where the valley-Zeeman $E_{\text{valley-Zeeman}} = - \int_{-\infty}^{\infty} B_z(y) m_K^{(0)}(y) dy$.

$m^{(1)}(y)$ is determined by the competition between valley-Zeeman interaction and intervalley coupling described in Eqn. (57). Then

$$m^{(1)}(y) \approx (|\alpha_K|^2 - |\beta_{K'}|^2) m_K^{(0)}(y) \tag{58}$$

Above, $(\alpha_K, \beta_{K'})^t$ denotes the eigenstate of H_{armchair} . The valley field has been taken to be approximately valley diagonal, as the off-diagonal part varies rapidly as $\exp(\pm i 2K y)$ and vanishes in a coarse grain average.

REFERENCES

- [1] K. S. Novoselov, A. K. Geim, S. V. Morozov, D. Jiang, M. I. Katsnelson, I. V. Grigorieva, S. V. Dubonos, and A. A. Firsov, *Nature* **438**, 197 (2005).
- [2] Y. Zhang, Y.-W. Tan, H. L. Stormer, and P. Kim, *Nature* **438**, 201 (2005).
- [3] A. H. Castro Neto, F. Guinea, N. M. R. Peres, K. S.

- Novoselov, and A. K. Geim, *Rev. Mod. Phys.* **81**, 109 (2009).
- [4] E. McCann and V. I. Fal'ko, *Phys. Rev. Lett.* **96**, 086805 (2006).
- [5] E. V. Castro, K. S. Novoselov, S. V. Morozov, N. M. R. Peres, J. M. B. L. dos Santos, J. Nilsson, F. Guinea, A. K. Geim, and A. H. C. Neto, *Phys. Rev. Lett.* **99**, 216802 (2007).
- [6] G. Giovannetti, P. A. Khomyakov, G. Brocks, P. J. Kelly, and J. van den Brink, *Phys. Rev. B* **76**, 073103 (2007).
- [7] B. Sachs, T. O. Wehling, M. I. Katsnelson, and A. I. Lichtenstein, *Phys. Rev. B* **84**, 195414 (2011).
- [8] K. F. Mak, C. Lee, J. Hone, J. Shan, and T. F. Heinz, *Phys. Rev. Lett.* **105**, 136805 (2010).
- [9] K. F. Mak, K. He, J. Shan, and T. F. Heinz, *Nature Nanotech* **7**, 494 (2012).
- [10] D. Xiao, W. Yao, and Q. Niu, *Phys. Rev. Lett.* **99**, 236809 (2007).
- [11] D. Xiao, G.-B. Liu, W. Feng, X. Xu, and W. Yao, *Phys. Rev. Lett.* **108**, 196802 (2012).
- [12] R. V. Gorbachev, J. C. W. Song, G. L. Yu, A. V. Kretinin, F. Withers, Y. Cao, A. Mishchenko, I. V. Grigorieva, K. S. Novoselov, L. S. Levitov, and A. K. Geim, *Science* **346**, 448 (2014).
- [13] Y. Shimazaki, M. Yamamoto, I. V. Borzenets, K. Watanabe, T. Taniguchi, and S. Tarucha, *Nature Phys* **11**, 1032 (2015).
- [14] M. Sui, G. Chen, L. Ma, W.-Y. Shan, D. Tian, K. Watanabe, T. Taniguchi, X. Jin, W. Yao, D. Xiao, and Y. Zhang, *Nature Phys* **11**, 1027 (2015).
- [15] Z. Wu, B. T. Zhou, X. Cai, P. Cheung, G.-B. Liu, M. Huang, J. Lin, T. Han, L. An, Y. Wang, S. Xu, G. Long, C. Cheng, K. T. Law, F. Zhang, and N. Wang, *Nat Commun* **10**, 611 (2019).
- [16] F. Zhang, A. H. MacDonald, and E. J. Mele, *Proceedings of the National Academy of Sciences* **110**, 10546 (2013).
- [17] I. Martin, Ya. M. Blanter, and A. F. Morpurgo, *Phys. Rev. Lett.* **100**, 036804 (2008).
- [18] L. Ju, Z. Shi, N. Nair, Y. Lv, C. Jin, J. Velasco, C. Ojeda-Aristizabal, H. A. Bechtel, M. C. Martin, A. Zettl, J. Analytis, and F. Wang, *Nature* **520**, 650 (2015).
- [19] J. Li, R.-X. Zhang, Z. Yin, J. Zhang, K. Watanabe, T. Taniguchi, C. Liu, and J. Zhu, *Science* **362**, 1149 (2018).
- [20] P. San-Jose and E. Prada, *Phys. Rev. B* **88**, 121408 (2013).
- [21] S. Huang, K. Kim, D. K. Efimkin, T. Lovorn, T. Taniguchi, K. Watanabe, A. H. MacDonald, E. Tutuc, and B. J. LeRoy, *Phys. Rev. Lett.* **121**, 037702 (2018).
- [22] P. Rickhaus, J. Wallbank, S. Slizovskiy, R. Pisoni, H. Overweg, Y. Lee, M. Eich, M.-H. Liu, K. Watanabe, T. Taniguchi, T. Ihn, and K. Ensslin, *Nano Lett.* **18**, 6725 (2018).
- [23] H. Zeng, J. Dai, W. Yao, D. Xiao, and X. Cui, *Nature Nanotech* **7**, 490 (2012).
- [24] T. Cao, G. Wang, W. Han, H. Ye, C. Zhu, J. Shi, Q. Niu, P. Tan, E. Wang, B. Liu, and J. Feng, *Nat Commun* **3**, 887 (2012).
- [25] P. Rivera, K. L. Seyler, H. Yu, J. R. Schaibley, J. Yan, D. G. Mandrus, W. Yao, and X. Xu, *Science* **351**, 688 (2016).
- [26] K. L. Seyler, P. Rivera, H. Yu, N. P. Wilson, E. L. Ray, D. G. Mandrus, J. Yan, W. Yao, and X. Xu, *Nature* **567**, 66 (2019).
- [27] G. Y. Wu, N.-Y. Lue, and L. Chang, *Phys. Rev. B* **84**, 195463 (2011).
- [28] A. Rycerz, J. Tworzydło, and C. W. J. Beenakker, *Nature Phys* **3**, 172 (2007).
- [29] C. Gold, A. Knothe, A. Kurzmann, A. Garcia-Ruiz, K. Watanabe, T. Taniguchi, V. Fal'ko, K. Ensslin, and T. Ihn, *Phys. Rev. Lett.* **127**, 046801 (2021).
- [30] N. Rohling and G. Burkard, *New J. Phys.* **14**, 083008 (2012).
- [31] Y. Wu, Q. Tong, G.-B. Liu, H. Yu, and W. Yao, *Phys. Rev. B* **93**, 045313 (2016).
- [32] G. Széchenyi, L. Chirolli, and A. Pályi, *2D Mater.* **5**, 035004 (2018).
- [33] J. Pawłowski, D. Żebrowski, and S. Bednarek, *Phys. Rev. B* **97**, 155412 (2018).
- [34] M.-K. Lee, N.-Y. Lue, C.-K. Wen, and G. Y. Wu, *Phys. Rev. B* **86**, 165411 (2012).
- [35] M. T. Allen, J. Martin, and A. Yacoby, *Nat Commun* **3**, 934 (2012).
- [36] A. Barreiro, H. S. J. van der Zant, and L. M. K. Vandersypen, *Nano Lett.* **12**, 6096 (2012).
- [37] L. Brey and H. A. Fertig, *Phys. Rev. B* **73**, 235411 (2006).
- [38] L. Jiao, L. Zhang, X. Wang, G. Diankov, and H. Dai, *Nature* **458**, 877 (2009).
- [39] D. V. Kosynkin, A. L. Higginbotham, A. Sinitskii, J. R. Lomeda, A. Dimiev, B. K. Price, and J. M. Tour, *Nature* **458**, 872 (2009).
- [40] J. Cai, P. Ruffieux, R. Jaafar, M. Bieri, T. Braun, S. Blankenburg, M. Muoth, A. P. Seitsonen, M. Saleh, X. Feng, K. Müllen, and R. Fasel, *Nature* **466**, 470 (2010).
- [41] L. Talirz, H. Söde, T. Dumsclaff, S. Wang, J. R. Sanchez-Valencia, J. Liu, P. Shinde, C. A. Pignedoli, L. Liang, V. Meunier, N. C. Plumb, M. Shi, X. Feng, A. Narita, K. Müllen, R. Fasel, and P. Ruffieux, *ACS Nano* **11**, 1380 (2017).
- [42] P. Ruffieux, S. Wang, B. Yang, C. Sánchez-Sánchez, J. Liu, T. Dienel, L. Talirz, P. Shinde, C. A. Pignedoli, D. Passerone, T. Dumsclaff, X. Feng, K. Müllen, and R. Fasel, *Nature* **531**, 489 (2016).
- [43] Z.-Z. Zhang, X.-X. Song, G. Luo, G.-W. Deng, V. Mosallanejad, T. Taniguchi, K. Watanabe, H.-O. Li, G. Cao, G.-C. Guo, F. Nori, and G.-P. Guo, *Sci. Adv.* **3**, e1701699 (2017).
- [44] K. Wang, K. De Greve, L. A. Jauregui, A. Sushko, A. High, Y. Zhou, G. Scuri, T. Taniguchi, K. Watanabe, M. D. Lukin, H. Park, and P. Kim, *Nature Nanotech* **13**, 128 (2018).
- [45] R. Pisoni, Z. Lei, P. Back, M. Eich, H. Overweg, Y. Lee, K. Watanabe, T. Taniguchi, T. Ihn, and K. Ensslin,

- Appl. Phys. Lett. **112**, 123101 (2018).
- [46] S. Shabani, D. Halbertal, W. Wu, M. Chen, S. Liu, J. Hone, W. Yao, D. N. Basov, X. Zhu, and A. N. Pasupathy, Nat. Phys. **17**, 720 (2021).
- [47] S. J. Magorrian, V. V. Enaldiev, V. Zólyomi, F. Ferreira, V. I. Fal'ko, and D. A. Ruiz-Tijerina, Phys. Rev. B **104**, 125440 (2021).
- [48] R. Pisoni, Y. Lee, H. Overweg, M. Eich, P. Simonet, K. Watanabe, T. Taniguchi, R. Gorbachev, T. Ihn, and K. Ensslin, Nano Lett. **17**, 5008 (2017).
- [49] A. Yu. Kitaev, Annals of Physics **303**, 2 (2003).
- [50] C. Nayak, S. H. Simon, A. Stern, M. Freedman, and S. Das Sarma, Rev. Mod. Phys. **80**, 1083 (2008).
- [51] C. W. J. Beenakker, Annual Review of Condensed Matter Physics **4**, 113 (2013).
- [52] S. D. Sarma, M. Freedman, and C. Nayak, Npj Quantum Inf **1**, 1 (2015).
- [53] C. L. Kane and E. J. Mele, Phys. Rev. Lett. **95**, 146802 (2005).
- [54] B. A. Bernevig and S.-C. Zhang, Phys. Rev. Lett. **96**, 106802 (2006).
- [55] M. König, S. Wiedmann, C. Brüne, A. Roth, H. Buhmann, L. W. Molenkamp, X.-L. Qi, and S.-C. Zhang, Science **318**, 766 (2007).
- [56] T. Cao, F. Zhao, and S. G. Louie, Phys. Rev. Lett. **119**, 076401 (2017).
- [57] D. J. Rizzo, G. Veber, T. Cao, C. Bronner, T. Chen, F. Zhao, H. Rodriguez, S. G. Louie, M. F. Crommie, and F. R. Fischer, Nature **560**, 204 (2018).
- [58] O. Gröning, S. Wang, X. Yao, C. A. Pignedoli, G. Borin Barin, C. Daniels, A. Cupo, V. Meunier, X. Feng, A. Narita, K. Müllen, P. Ruffieux, and R. Fasel, Nature **560**, 209 (2018).
- [59] K.-S. Lin and M.-Y. Chou, Nano Lett. **18**, 7254 (2018).
- [60] M. S. Dresselhaus, G. Dresselhaus, and A. Jorio, *Group Theory: Application to the Physics of Condensed Matter* (Springer-Verlag, Berlin, 2008).
- [61] A. Kitaev, AIP Conference Proceedings **1134**, 22 (2009).
- [62] X.-L. Qi and S.-C. Zhang, Rev. Mod. Phys. **83**, 1057 (2011).
- [63] A. Einstein, B. Podolsky, and N. Rosen, Phys. Rev. **47**, 777 (1935).
- [64] J. S. Bell, Physics Physique Fizika **1**, 195 (1964).
- [65] J. F. Clauser, M. A. Horne, A. Shimony, and R. A. Holt, Phys. Rev. Lett. **23**, 880 (1969).
- [66] A. Aspect, P. Grangier, and G. Roger, Phys. Rev. Lett. **47**, 460 (1981).
- [67] G. Weihs, T. Jennewein, C. Simon, H. Weinfurter, and A. Zeilinger, Phys. Rev. Lett. **81**, 5039 (1998).
- [68] L. D. Landau and E. M. Lifshitz, *Statistical Physics*, Third Edition, Vol. Part 1 (Elsevier Science & Technology, Oxford, 1996).
- [69] J. D. Jackson, *Classical Electrodynamics*, Third Edition (New York, 1998).
- [70] R. Peierls, Z. Physik **80**, 763 (1933).
- [71] P. R. Wallace, Phys. Rev. **71**, 622 (1947).
- [72] G.-B. Liu, W.-Y. Shan, Y. Yao, W. Yao, and D. Xiao, Phys. Rev. B **88**, 085433 (2013).
- [73] K. V. Shanavas and S. Satpathy, Phys. Rev. B **91**, 235145 (2015).
- [74] F.-W. Chen and Y.-S. G. Wu, Phys. Rev. Research **2**, 013076 (2020).
- [75] W. Feng, Y. Yao, W. Zhu, J. Zhou, W. Yao, and D. Xiao, Phys. Rev. B **86**, 165108 (2012).
- [76] A. Lopez-Bezanilla and J. L. Lado, Phys. Rev. Research **2**, 033357 (2020).
- [77] S. Wu, J. S. Ross, G.-B. Liu, G. Aivazian, A. Jones, Z. Fei, W. Zhu, D. Xiao, W. Yao, D. Cobden, and X. Xu, Nature Phys **9**, 149 (2013).
- [78] E. Liu, E. Barré, J. van Baren, M. Wilson, T. Taniguchi, K. Watanabe, Y.-T. Cui, N. M. Gabor, T. F. Heinz, Y.-C. Chang, and C. H. Lui, Nature **594**, 46 (2021).
- [79] A. Weston, Y. Zou, V. Enaldiev, A. Summerfield, N. Clark, V. Zólyomi, A. Graham, C. Yelgel, S. Magorrian, M. Zhou, J. Zultak, D. Hopkinson, A. Barinov, T. H. Bointon, A. Kretinin, N. R. Wilson, P. H. Beton, V. I. Fal'ko, S. J. Haigh, and R. Gorbachev, Nat. Nanotechnol. **15**, 592 (2020).
- [80] A. Weston, E. G. Castanon, V. Enaldiev, F. Ferreira, S. Bhattacharjee, S. Xu, H. Corte-León, Z. Wu, N. Clark, A. Summerfield, T. Hashimoto, Y. Gao, W. Wang, M. Hamer, H. Read, L. Fumagalli, A. V. Kretinin, S. J. Haigh, O. Kazakova, A. K. Geim, V. I. Fal'ko, and R. Gorbachev, Nat. Nanotechnol. **17**, 390 (2022).